Energy Landscapes: From Clusters to Supercooled Liquids and Glasses

David J. Wales

University Chemical Laboratories, Lensfield Road, Cambridge CB2 1EW, UK

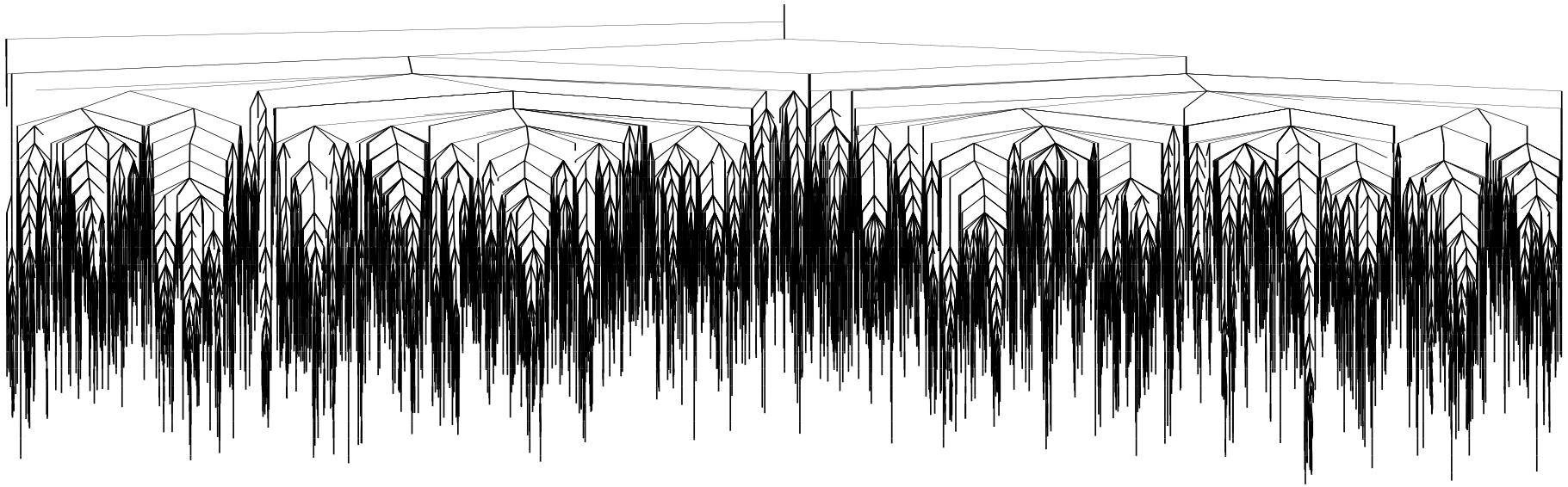

Books and Reviews

'Energy Landscapes', D. J. Wales, CUP, 2003

Chem. Phys. Lett., **466**, 105, 2008; J. Phys. Chem. B, **110**, 20765, 2006

Int. Rev. Phys. Chem., **25**, 237, 2006; Adv. Chem. Phys., **115**, 1, 2000

§1 Introduction

In classical mechanics the potential energy function, V, determines the structure, dynamics and thermodynamics of any system.

Stable configurations occur at minima in V, defining the structure; the gradient of V gives (minus) the forces on the particles, which appear in the equations of motion; and the configuration integral, which determines the thermodynamics, is also a function of V.

Analogous statements can be made in quantum mechanics within the Born–Oppenheimer approximation, where the potential energy surface (PES) is the solution of the Schrödinger equation for frozen nuclear positions.

Observable properties are determined by the topology and topography of the 'potential energy landscape', or just the 'energy landscape'.[1] The latter expression is also used to refer to free energy, though this should be clear from the context.

As the size of the system increases, so does the dimensionality of the configuration space required to describe it.

In the late 1960's the first attempts were being made to predict the three-dimensional structure of globular proteins from their amino acid sequence.

Anfinsen had shown that some denatured proteins regained their native structure reliably on a laboratory time scale.

By coarse-graining configuration space, Levinthal realised that the number of possible conformations for a typical protein is astronomically large. If they were searched at random on the fastest vibration time scale the time required to find the native state would exceed the lifetime of the universe.

This discrepancy is known as Levinthal's paradox, and similar 'paradoxes' can be constructed for self-assembly, crystallisation, and the appearance of magic numbers for clusters in a molecular beam. The study of energy landscapes enables us to unify and explain these apparently diverse phenomena.

§2 Disconnectivity Graphs

Disconnectivity graphs provide a powerful way to visualise the PES from a database of stationary points (Becker and Karplus).[2,3]

At a given total energy, E, the minima can be grouped into disjoint sets, whose members are mutually accessible at that energy: each pair of minima in a set is connected directly or indirectly by a path with energy $< E$. Connected graphs that contain no cycles are known as 'trees'.

'palm tree' 'weeping willow' 'banyan tree'

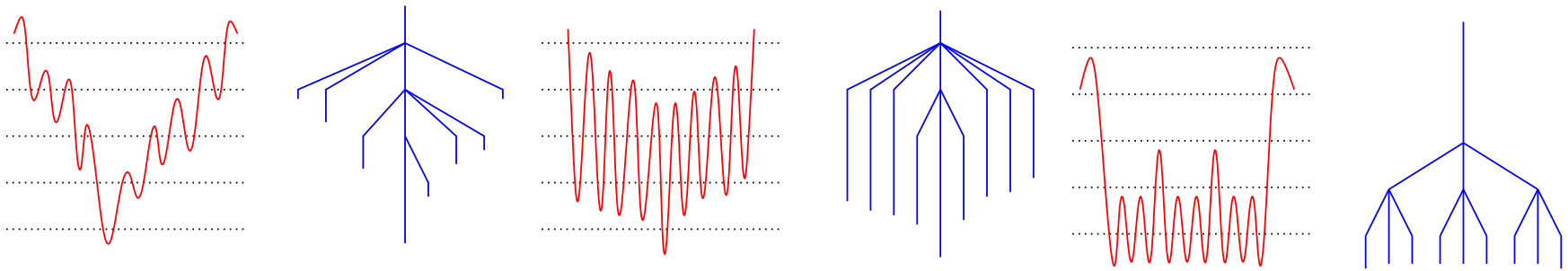

Catastrophe theory explains why short-range potentials result in surfaces that are globally flatter but locally rougher, while long-range potentials produce potential energy funnels and efficient local relaxation.[4]

§2.1 Landscapes with Funnelling Properties

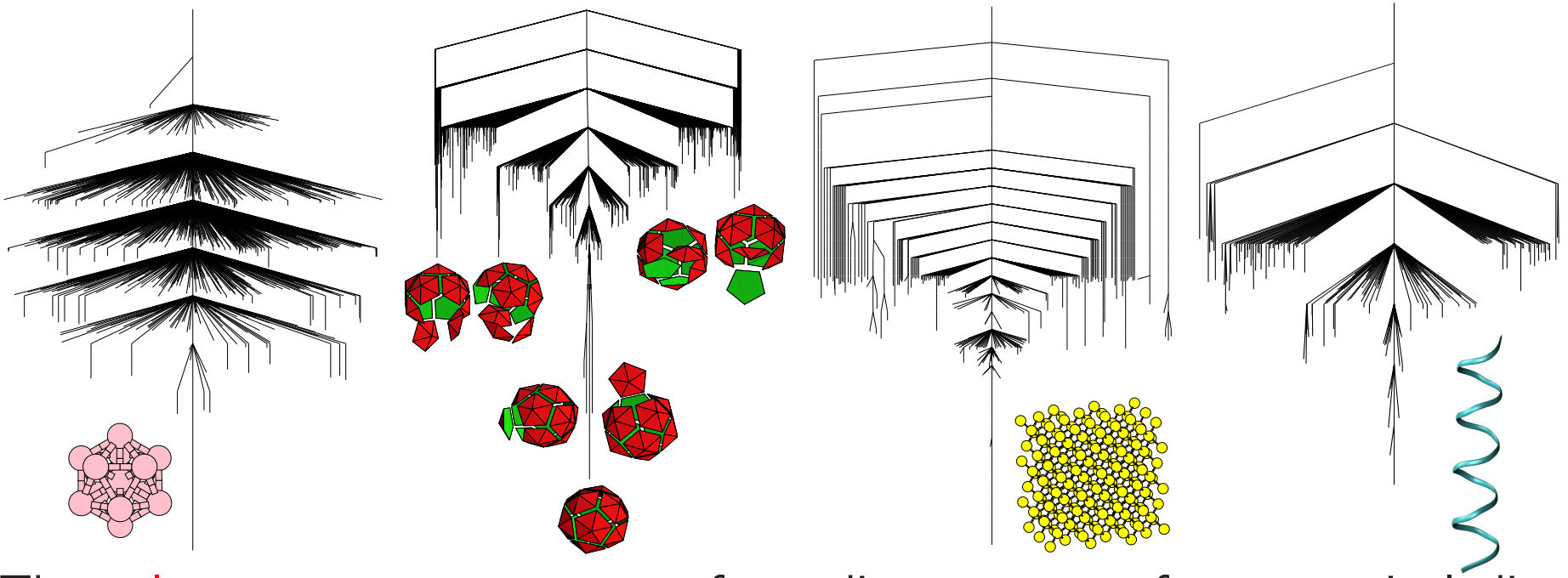

The palm tree structure appears for a diverse range of systems, including the LJ_{13} cluster, icosahedral shells composed of pentagonal and hexagonal pyramids, crystalline (Stillinger-Weber) silicon, and the polyalanine ala_{16}.

We associate this pattern with 'funnelling' properties, minimal frustration, large T_f/T_g, or hierarchical constraints. Such landscapes may guide the non-random searches that result in magic number clusters, crystallisation, self-assembly, and protein folding.[1,5,6]

§2.2 A Double-Funnel System: LJ_{38}

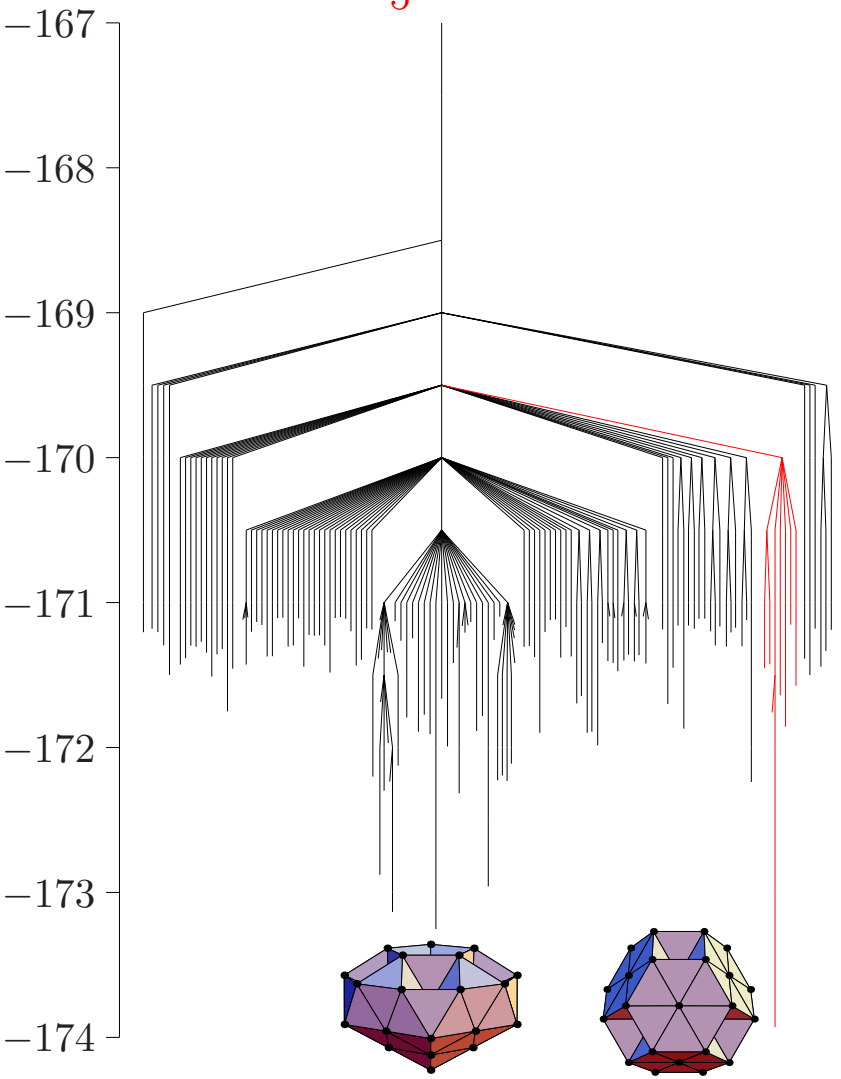

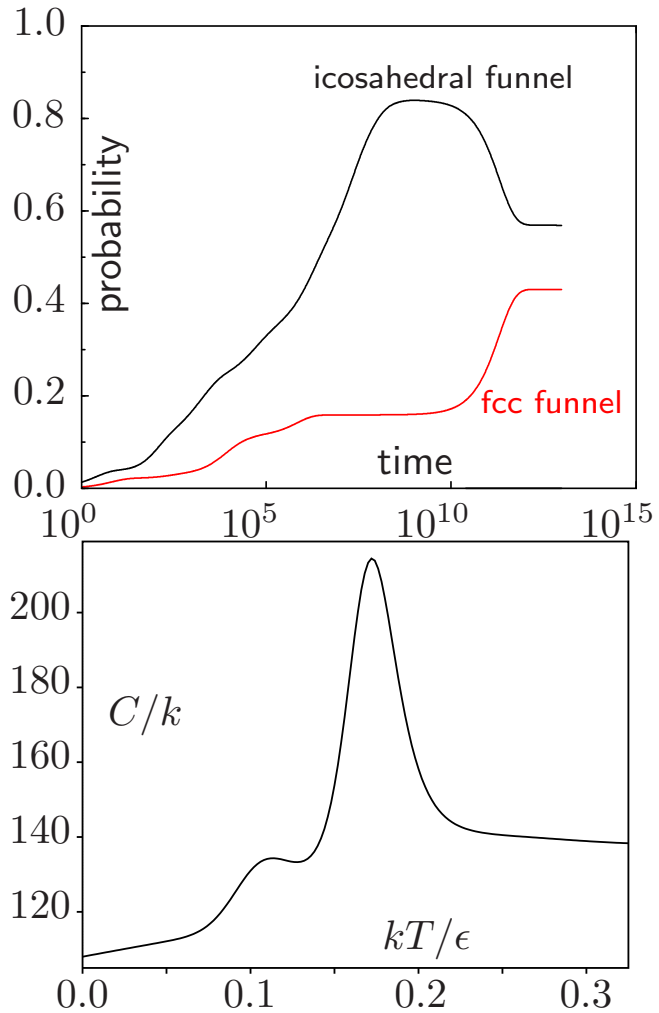

LJ_{38} exhibits a double funnel due to competition between icosahedral and truncated octahedral morphologies. The interconversion rate for Ar_{38} is calculated as $55\,s^{-1}$ at 14 K where a solid-solid transition occurs.

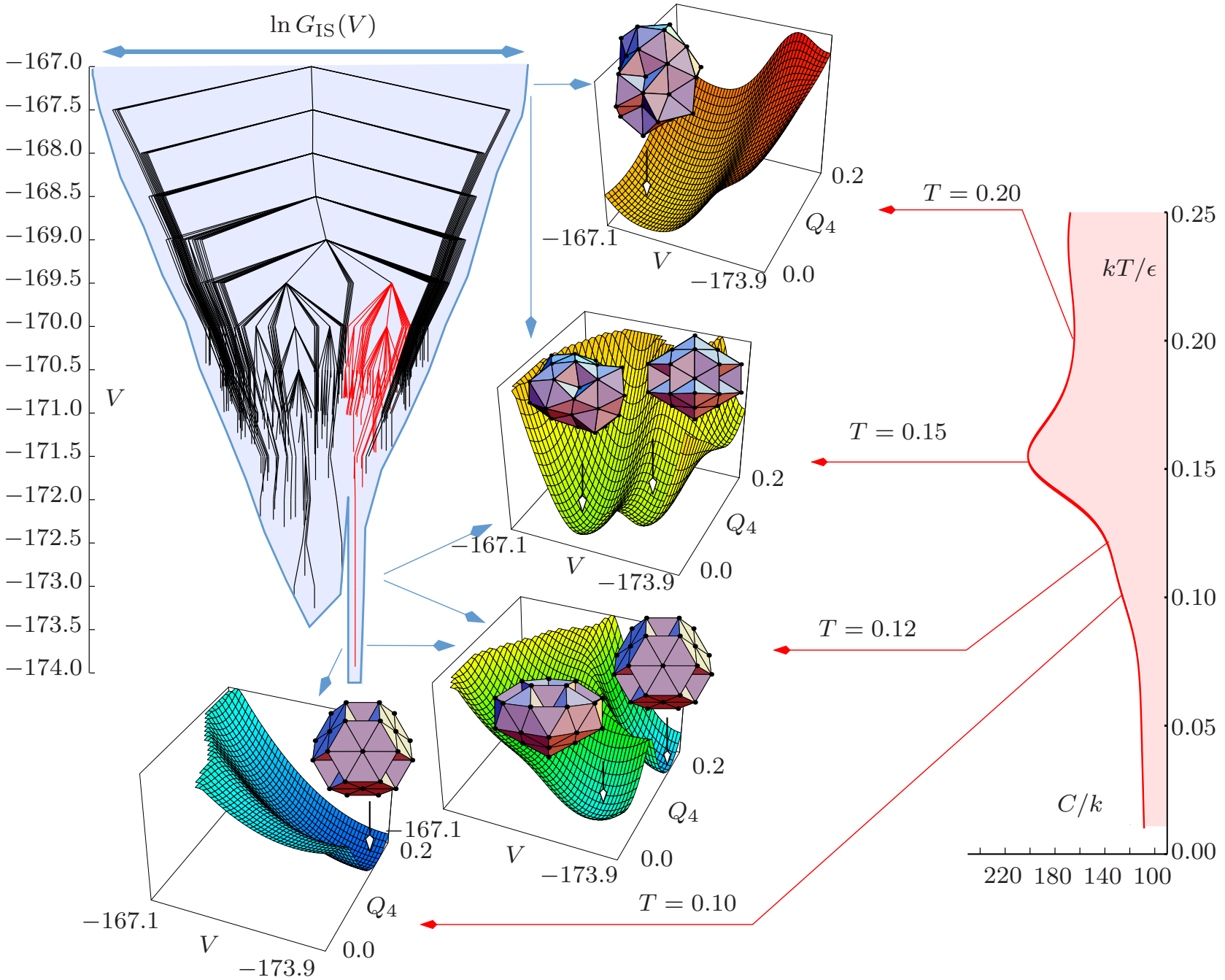

The solid-solid transition produces a heat capacity feature.

§2.3 Annealing of C_{60}

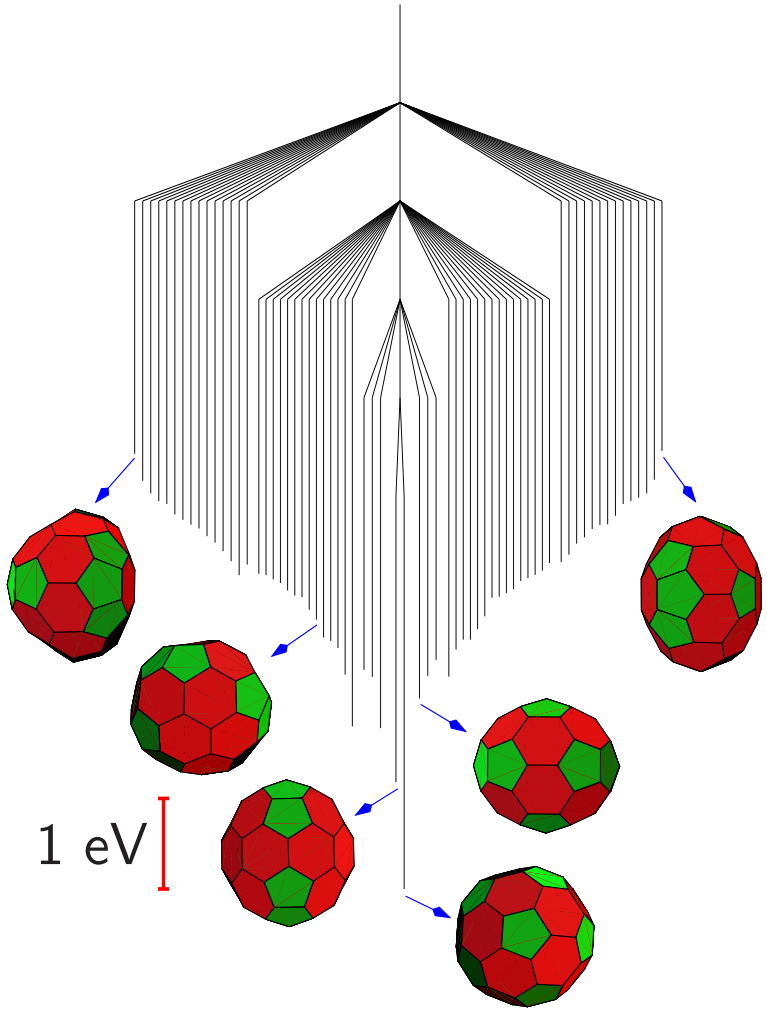

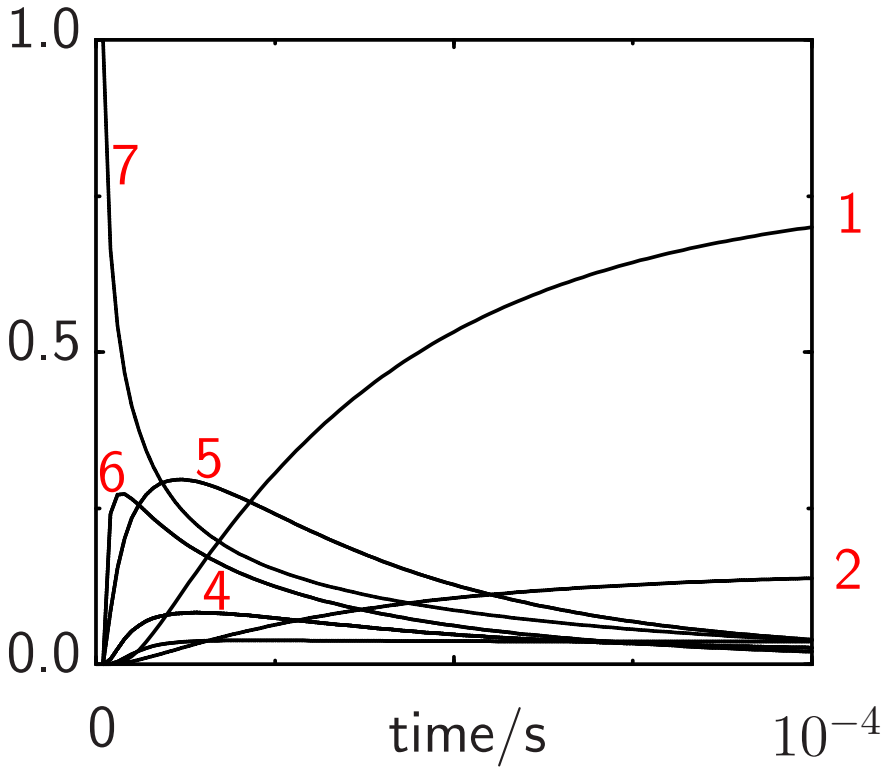

For C_{60} the long branches correspond to high barriers $\sim 4\,\mathrm{eV}$ (left). Relaxation from high energy to the icosahedral global minimum occurs on a time scale of milliseconds if the temperature is high enough (right).

§2.4 A Model Protein

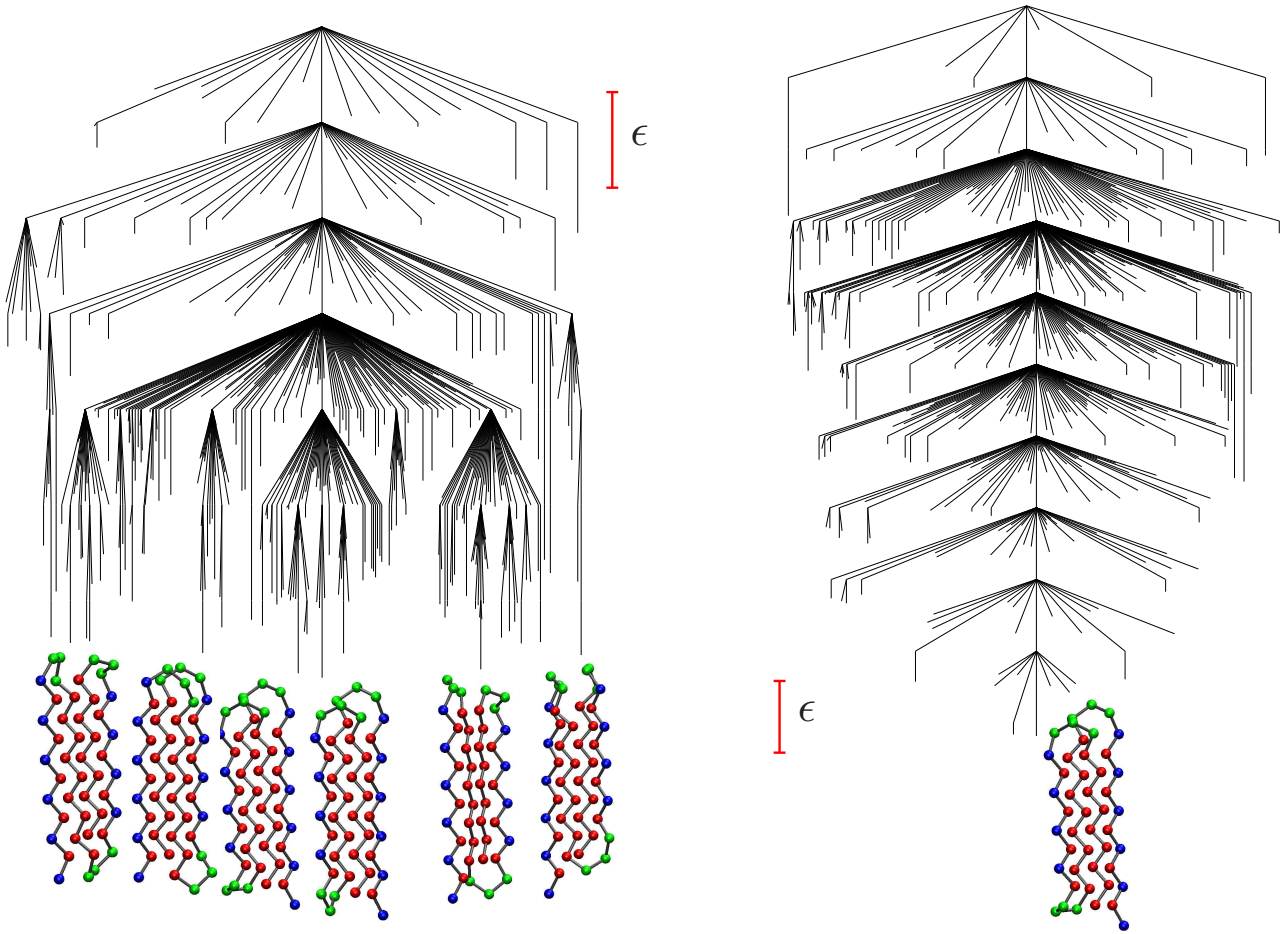

The global minimum of the off-lattice bead model $\mathrm{B_9N_3(LB)_4N_3B_9N_3(LB)_5L}$ is a four-stranded β-barrel, where B=hydrophobic, L=hydrophilic, and N=neutral. The original system exhibits frustration, which is eliminated in the corresponding Gō model (and reduced by salt bridges).[7,8]

§2.5 $(H_2O)_{20}$: A Molecular Cluster

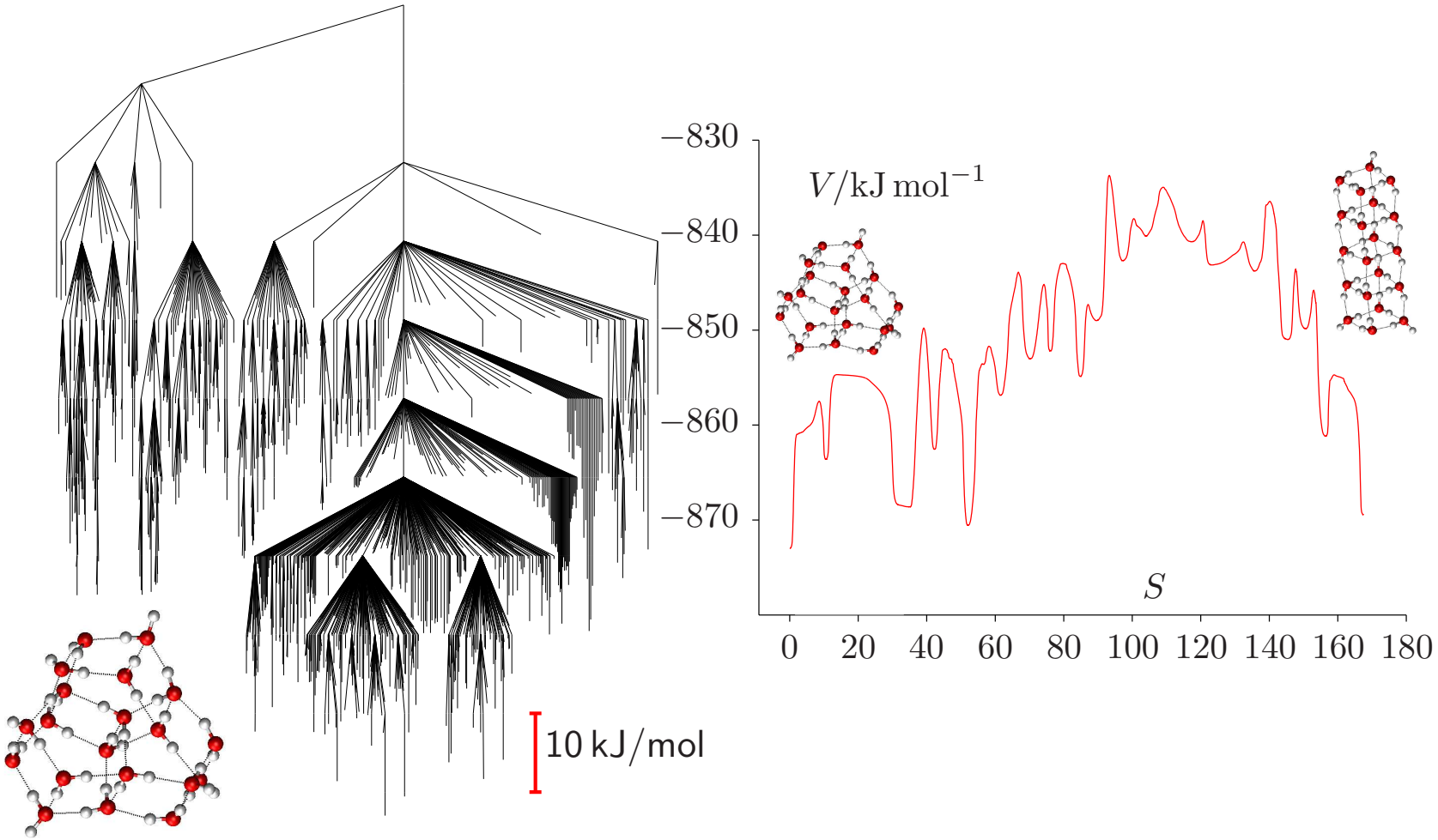

A disconnectivity graph for TIP4P $(H_2O)_{20}$ exhibits hierarchical structure: sets of minima are disconnected together.[3] The interconversion rate between the pentagonal prism and box-kite morphologies at 40 K is around 10^{-37} s^{-1}.

§3 Geometry Optimisation

Finding local minima is usually straightforward. There are several efficient standard techniques available that require only gradient information.

Second derivatives can be useful for transition state searches, where we must locate a stationary point that is a local maximum in one principal direction but a local minimum in the others.

Consider the Taylor expansion of the potential energy around a general point in nuclear configuration space, $\mathbf{X}$, truncated at second order:

$$V(\mathbf{X}+\mathbf{x}) = \mathbf{V}(\mathbf{X}) + \mathbf{G}(\mathbf{X})^{\mathbf{T}}\,\mathbf{x} + \frac{\mathbf{1}}{\mathbf{2}}\mathbf{x}^{\mathbf{T}}\,\mathbf{H}(\mathbf{X})\,\mathbf{x}, \qquad (1)$$

where $\mathbf{G}(\mathbf{X})$ and $\mathbf{H}(\mathbf{X})$ are the gradient and Hessian, and $\mathbf{x}$ is a vector of small nuclear displacements.

Applying $d\mathbf{V}(\mathbf{X}+\mathbf{x})/\mathbf{dx} = \mathbf{0}$ leads to the Newton-Raphson step:

$$\mathbf{x}_{\mathrm{NR}} = -\mathbf{H}^{-1}\mathbf{G}. \tag{2}$$

However, the inverse Hessian is usually undefined due to zero eigenvalues. Since each eigenvector, $\mathbf{e}$, corresponding to overall translation or rotation is known, the corresponding eigenvalues can be shifted arbitrarily by adding a multiple of $\hat{e}_\alpha \hat{e}_\beta$ to $H_{\alpha\beta}$.

In normal mode coordinates $\mathbf{x}_{\mathrm{NR}}$ and the energy change ΔV_{NR} are

$$x_{\mathrm{NR},\alpha} = -g_\alpha/\varepsilon_\alpha^2 \quad \text{and} \quad \Delta V_{\mathrm{NR}} = -\sum_{\alpha=1}^{3N} g_\alpha^2/2\varepsilon_\alpha^2.$$

Hence contributions from terms with Hessian eigenvalues $\varepsilon_\alpha^2 > 0$ and $\varepsilon_\alpha^2 < 0$ lower and raise the energy, respectively.

Newton-Raphson searches can converge to stationary points of any Hessian index (defined as the number of negative eigenvalues of $\mathbf{H}$).

§3.1 Locating Transition States: Eigenvector-Following

With only a little extra effort it is possible to obtain an algorithm that will systematically converge to a stationary point of any required index.

Introducing an additional Lagrange multiplier gives increased flexibility, which can be exploited to find transition states systematically:

$$L = -v(\mathbf{W}) - \sum_{\alpha=1}^{3N} \left[g_\alpha(\mathbf{W})\, x_\alpha + \frac{1}{2}\varepsilon_\alpha^2\, x_\alpha^2 - \frac{1}{2}\mu_\alpha (x_\alpha^2 - c_\alpha^2) \right].$$

The step that is optimal in all directions is now

$$x_\alpha = g_\alpha(\mathbf{W})/(\mu_\alpha - \varepsilon_\alpha^2),$$

and the energy change corresponding to this step is

$$\Delta V = \sum_{\alpha=1}^{3N} (\mu_\alpha - \varepsilon_\alpha^2/2) g_\alpha(\mathbf{W})^2/(\mu_\alpha - \varepsilon_\alpha^2)^2.$$

Now we must make a choice for μ_α. We require $\mu_\alpha \to 0$ as $g_\alpha(\mathbf{W}) \to 0$, so that the Newton-Raphson step is recovered.

We also need $\mu_\alpha - \varepsilon_\alpha^2/2 < 0$ for minimisation and $\mu_\alpha - \varepsilon_\alpha^2/2 > 0$ for maximisation. Effective choices for μ_α have been found through a combination of theory and experiment. For example

$$\mu_\alpha = \varepsilon_\alpha^2 \pm \frac{1}{2}|\varepsilon_\alpha^2| \left(1 + \sqrt{1 + 4g_\alpha(\mathbf{W})^2/\varepsilon_\alpha^4}\right),$$

plus for maximisation, minus for minimisation, gives steps that obey the required conditions and are an even function of ε_α^2.

A graphical comparison is possible for a simple triatomic cluster.[9,10] Every pixel in each of the plots corresponds to a particular geometry in a cut through the three-dimensional configuration space of a three-atom cluster. The colour depends upon which stationary point the algorithm in question converges to and the resolution is 700×700.

The Newton-Raphson algorithm can converge to both minima and transition states, depending upon where we start from:

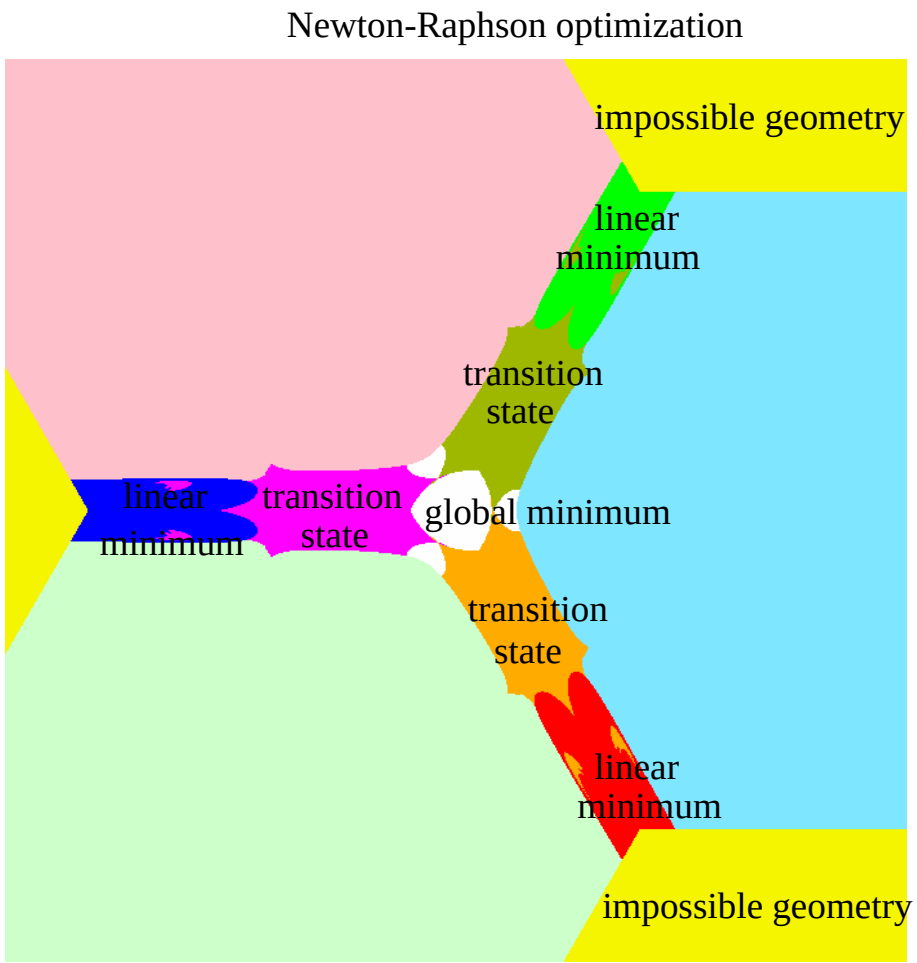

Geometry optimisation may not yield the 'nearest' stationary point in terms of a distance metric.

The eigenvector-following method converges only to stationary points of the specified index, i.e. minima (left) and transition states (right):

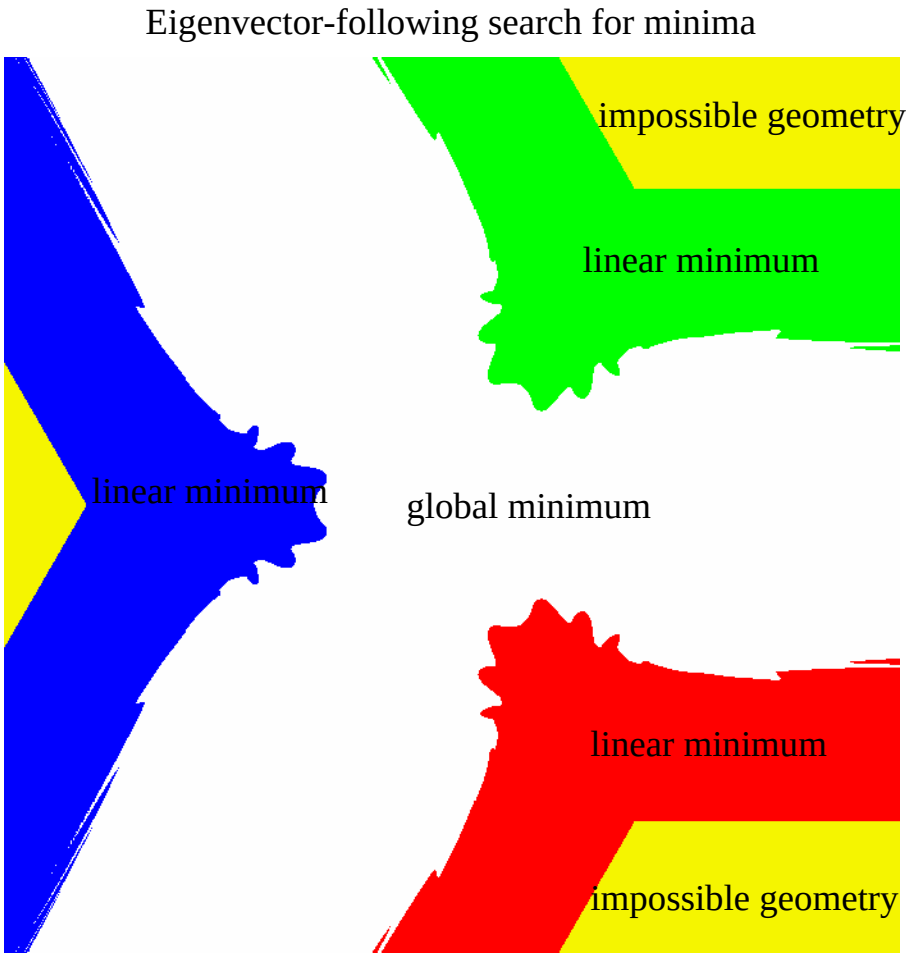

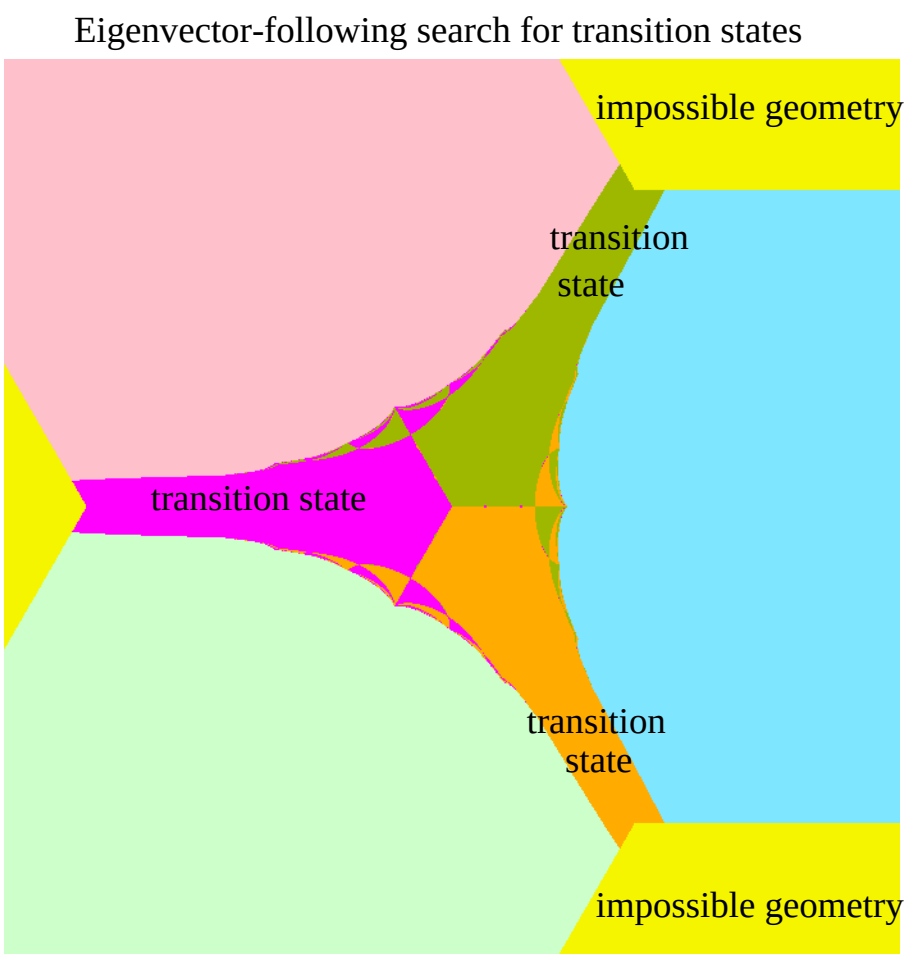

§3.2 Hybrid Eigenvector-Following

In hybrid eigenvector-following an uphill eigenvector-following step is taken in one eigendirection and minimisation is performed in the tangent space.[11]

Second derivatives are not required if the eigenvector and eigenvalue are calculated using a variational approach,[11] defining $\lambda(\mathbf{x}) = \mathbf{x}^T \mathbf{H}\,\mathbf{x}/\mathbf{x}^2$.

Second derivatives are avoided by formulating $\lambda(\mathbf{x})$ as[11–13]

$$\lambda(\mathbf{x}) \approx \frac{V(\mathbf{X}+\xi\mathbf{x}) + V(\mathbf{X}-\xi\mathbf{x}) - 2V(\mathbf{X})}{(\xi\mathbf{x})^2},$$

$$\text{with} \quad \frac{\partial\lambda(\mathbf{x})}{\partial\mathbf{x}} = \frac{\nabla V(\mathbf{X}+\xi\mathbf{x}) - \nabla V(\mathbf{X}-\xi\mathbf{x})}{\xi\mathbf{x}^2} - \frac{2\lambda(\mathbf{x})\mathbf{x}}{\mathbf{x}^2}.$$

Once the smallest eigenvalue and the corresponding eigenvector are known transition states can be found using eigenvector-following for the uphill step and minimisation in the tangent space. Example: Si defect migration.[14]

Eigenvector-following techniques can easily be adapted to locate stationary points of any given Hessian index systematically.[15]

This approach is much more efficient than minimising $|\nabla V|^2$, which can converge to a stationary point of any index, and to non-stationary points (NSPs)[15–17] where the gradient is an eigenvector of the Hessian with zero eigenvalue and $|\nabla V|^2 > 0$.

Convergence to NSPs is slow because the additional zero eigenvalue leads to a singular condition number.

The basins of attraction for NSPs dominate the $|\nabla V|^2$ surface for the simple two-dimensional Müller-Brown surface, and this effect is even more pronounced for larger systems.[15–17]

Fortunately, only local minima and saddle points of index one are required in the energy landscapes formulation of global thermodynamics (§5) and kinetics (§6).

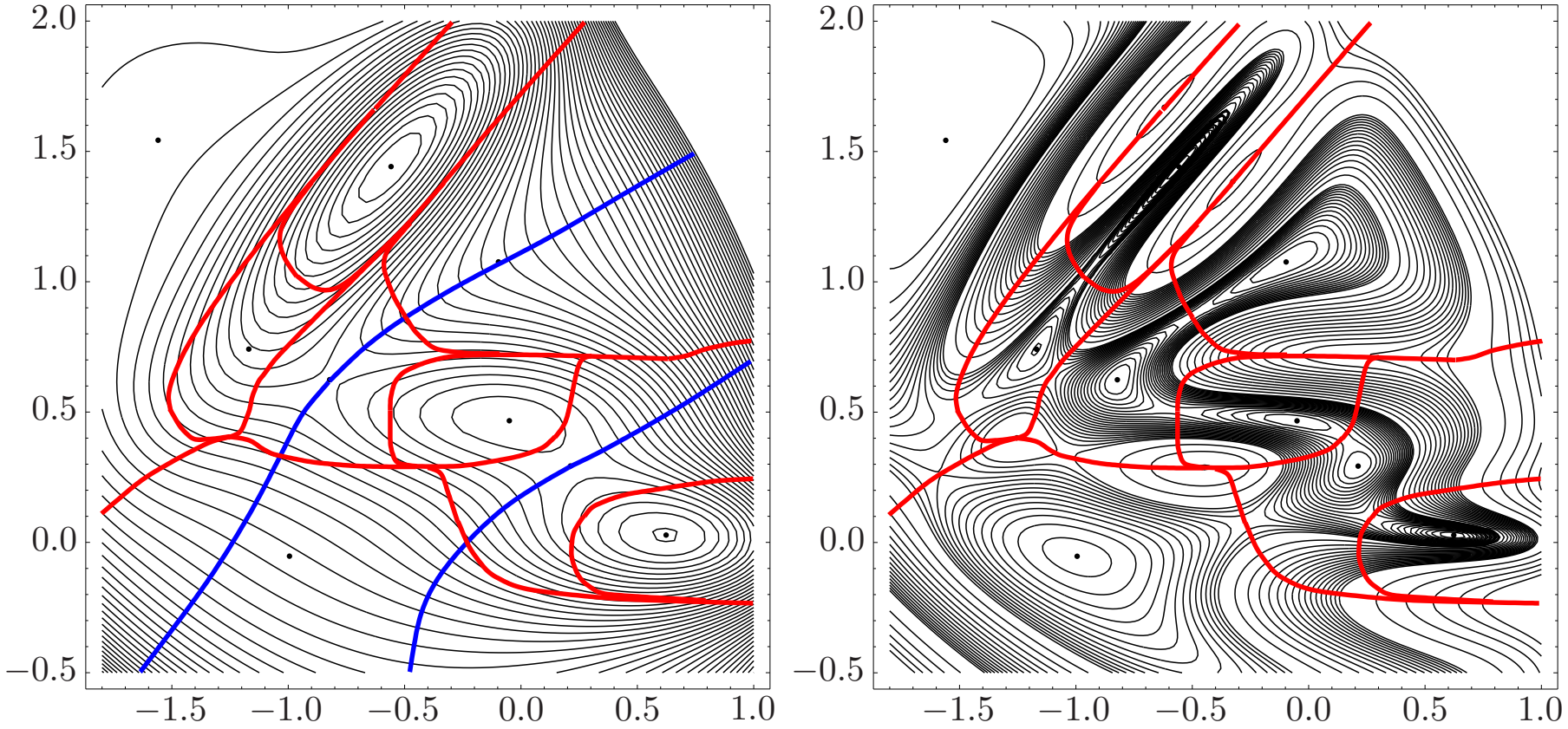

Contour plots of V (left) and $|\nabla V|^2$ (right) for the Müller-Brown surface.[18] Blue and red lines define the basins of attraction for minima of V and $|\nabla V|^2$.[15] The points correspond to minima of $|\nabla V|^2$ (left) and to the maxima and minima of $|\nabla V|^2$ (right).

Nudged and Doubly-Nudged Elastic Bands

Double-ended chain-of-states methods[19–21] have evolved into nudged[22,23] and doubly-nudged[24] elastic band approaches.

Pathways are characterised by considering images of the system at intermediate geometries, $\mathbf{X}_i$, and supplementing the true gradient, $\mathbf{g}$, with an attractive spring gradient, $\widetilde{\mathbf{g}}$, between adjacent images.

Corner-cutting is significant when a path experiences high curvature. The images cannot follow the path accurately because the spring force has a large component perpendicular to the tangent, $\widetilde{\mathbf{g}}^{\perp}$.

Sliding-down occurs due to $\mathbf{g}^{\parallel}$, which perturbs the distribution of images along the path, creating high-resolution regions around the local minima and low-resolution regions near the transition states.

Nudging projects out $\mathbf{g}^{\parallel}$ and $\widetilde{\mathbf{g}}^{\perp}$, and optimising the images produces transition state candidates for accurate refinement by hybrid eigenvector-following.

§3.3 Finding an Initial Discrete Path for Distant Minima[25]

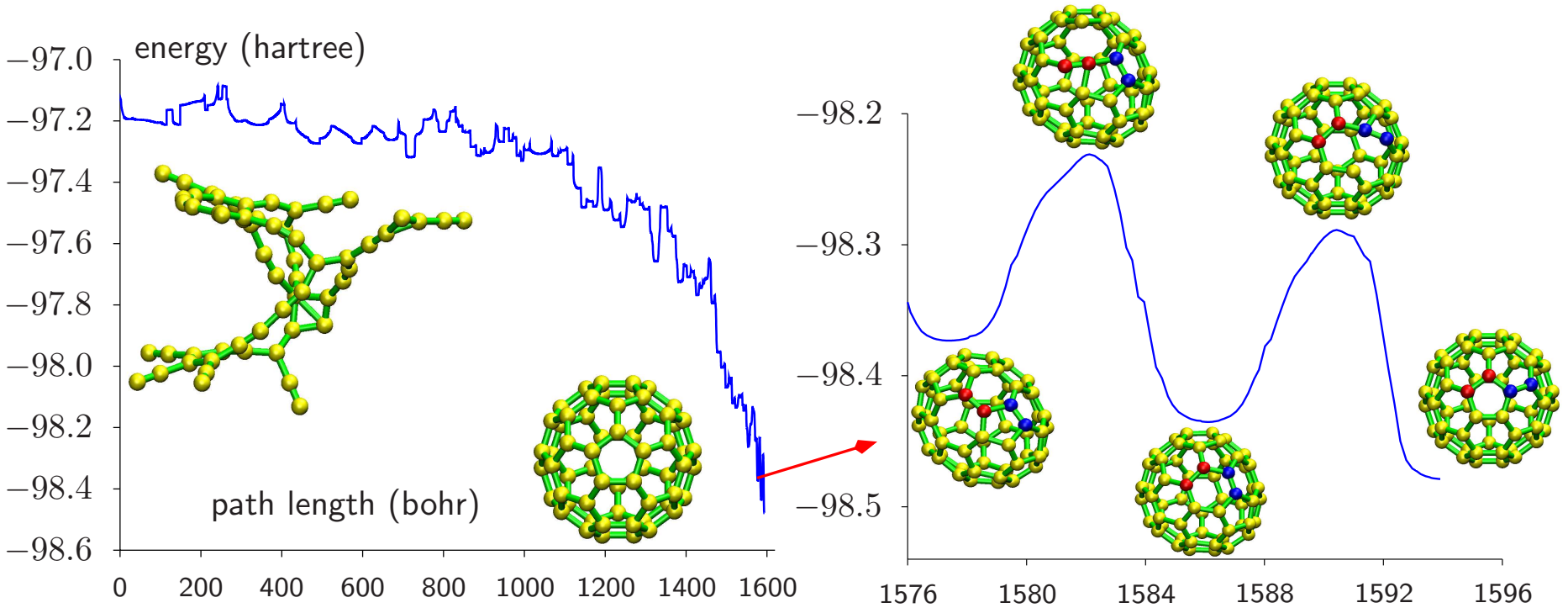

Distant local minima can be connected by successive transition state searches using Dijkstra's algorithm to choose the next pair of minima, avoiding a combinatorial problem.[25]

This C_{60} path from a random network to buckminsterfullerene contains 82 transition states, and required 383 cycles of the Dijkstra missing connection algorithm, including 1620 DNEB searches, for a tight-binding potential.

§4 Basin-Hopping Global Optimisation[26]

In treating any non-trivial global optimisation problem, the principal difficulty arises from the exponentially large number of minima on the PES.

There is a simple transformation of the energy landscape that does not change the global minimum, or the relative energies of any local minima:

$$\widetilde{E}(\mathbf{X}) = \min\{E(\mathbf{X})\}, \tag{3}$$

where 'min' signifies that an energy minimisation is carried out starting from $\mathbf{X}$. The transformed energy, $\widetilde{E}(\mathbf{X})$, at any point, $\mathbf{X}$, becomes the energy of the structure obtained by minimisation.

Each local minimum is, therefore, surrounded by a catchment basin of constant energy consisting of all the neighbouring geometries from which that particular minimum is obtained.

The catchment basin transformation removes all the transition state regions from the surface and accelerates the dynamics because the system can pass between basins all along their boundary. Atoms can even pass through each other without encountering prohibitive energy barriers.

The basin-hopping approach therefore transforms the energy landscape to a discrete set of energy levels corresponding to the energies of local minima, and must be combined with a search strategy.

In the 'Monte Carlo plus energy minimisation' procedure steps are proposed by perturbing the current coordinates and carrying out a minimisation from the resulting geometry.

A step is accepted if the energy of the new minimum, E_{new}, is lower than the starting point, E_{old}. If $E_{\mathrm{new}} > E_{\mathrm{old}}$ then the step is accepted if $\exp[(E_{\mathrm{old}} - E_{\mathrm{new}})/kT]$ is greater than a random number drawn from the interval [0,1]. The temperature, T, becomes an adjustable parameter.

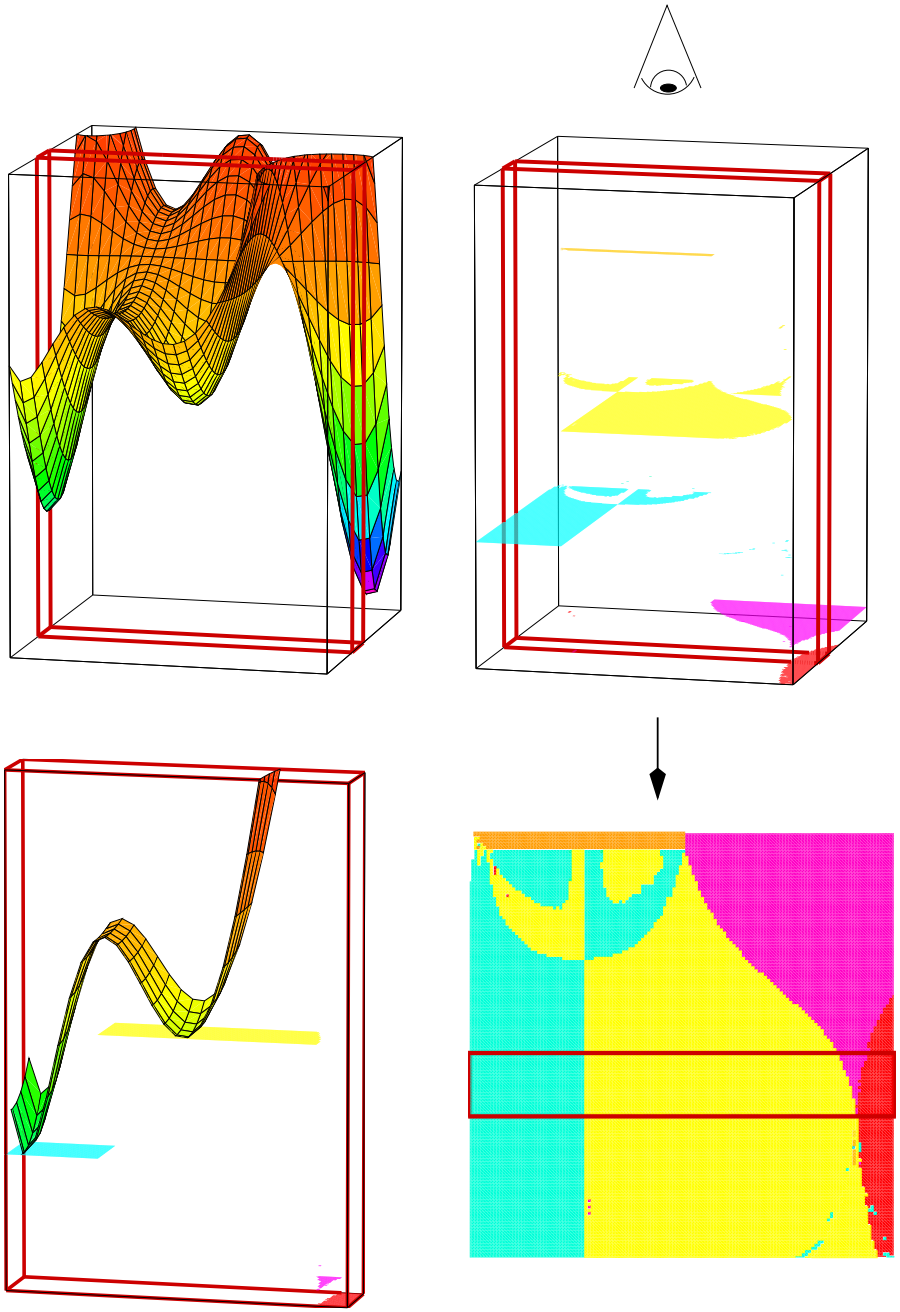

Illustration of the $\widetilde{E}(\mathbf{X})$ energy landscape transformation.

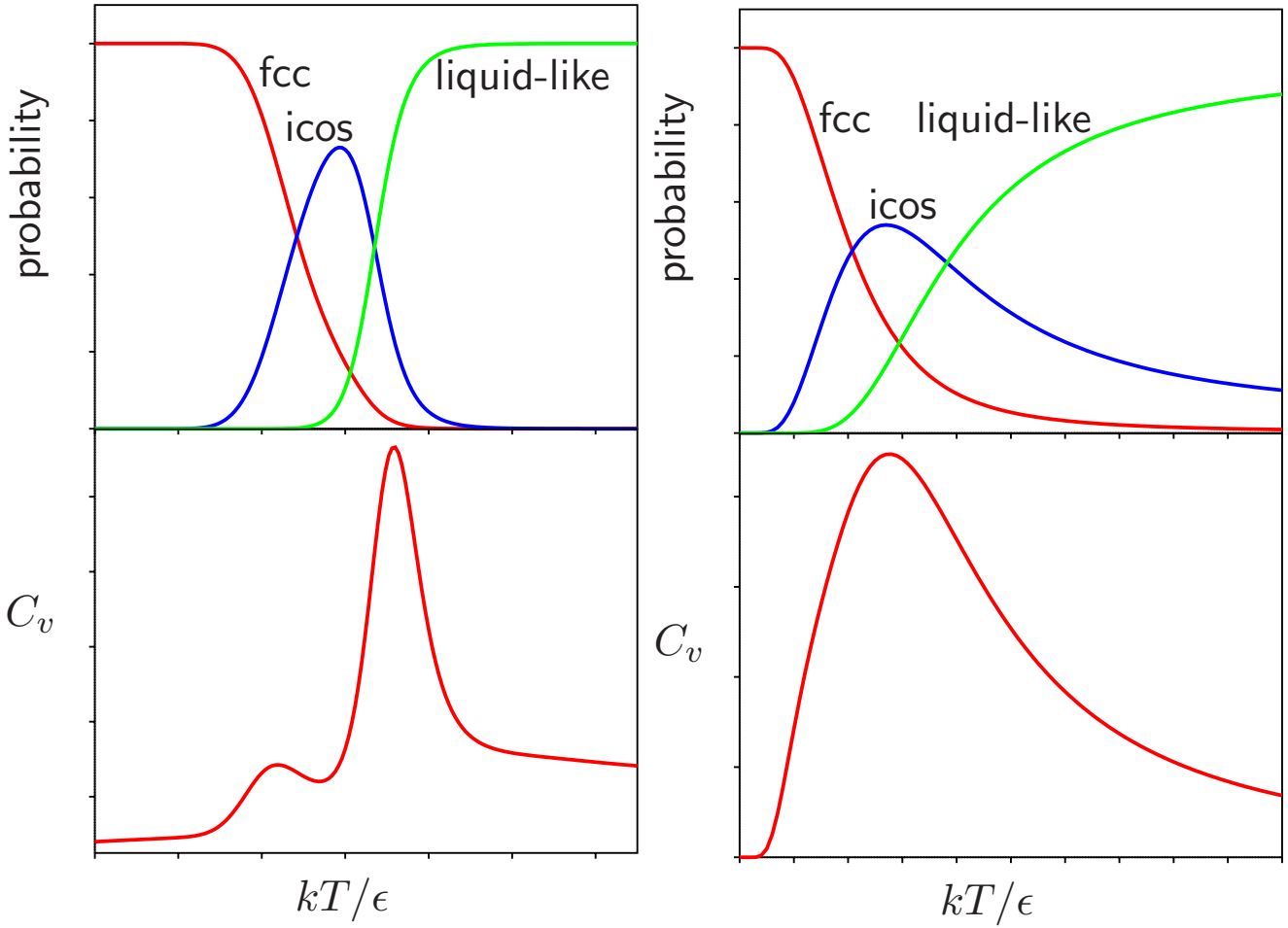

Basin-hopping succeeds for multi-funnel surfaces because the transitions are broadened,[27] giving a larger overlap in the probability distributions of different morphologies (right panels). (cf. Tsallis statistics, non-Boltzmann sampling).

Examples from the Cambridge Cluster Database

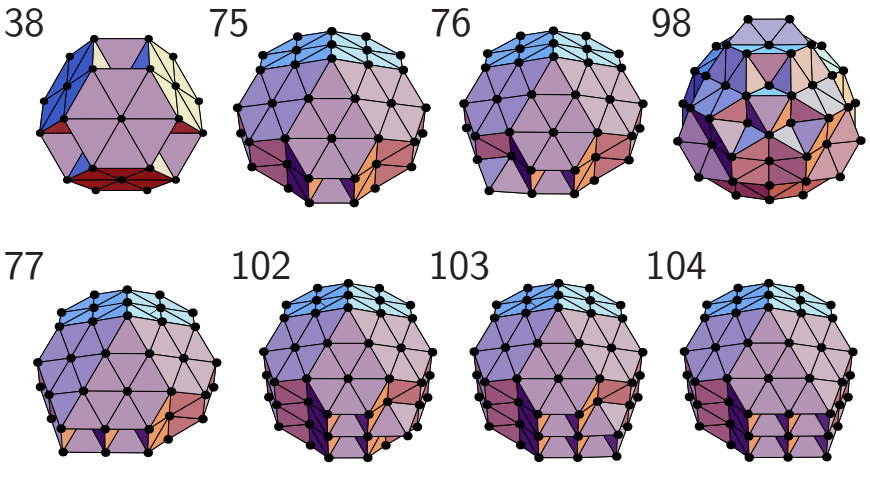

Non-icosahedral Lennard-Jones Clusters

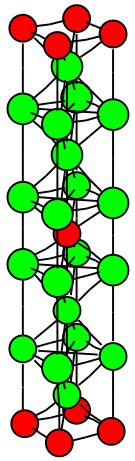

Binary LJ unit cell

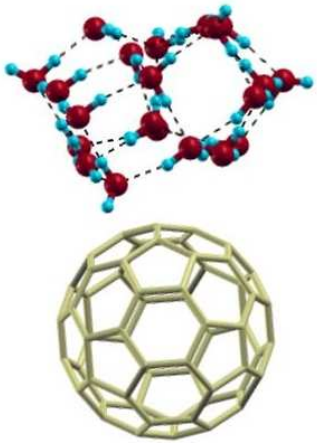

$C_{60}(H_2O)_{20}$

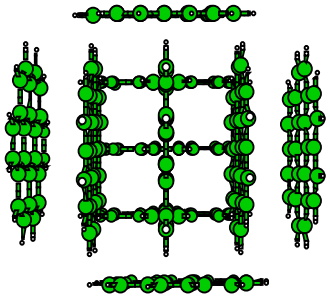

$corronene_{10}$

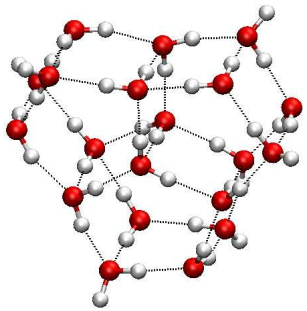

$(H_2O)_{20}$

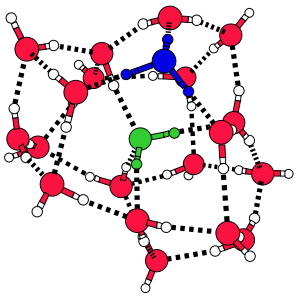

$H_3O^+(H_2O)_{20}$ Eigen

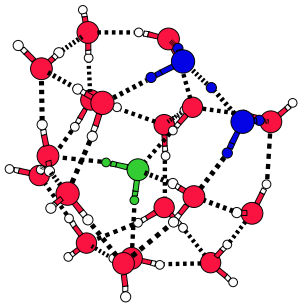

$H_3O^+(H_2O)_{20}$ Zundel

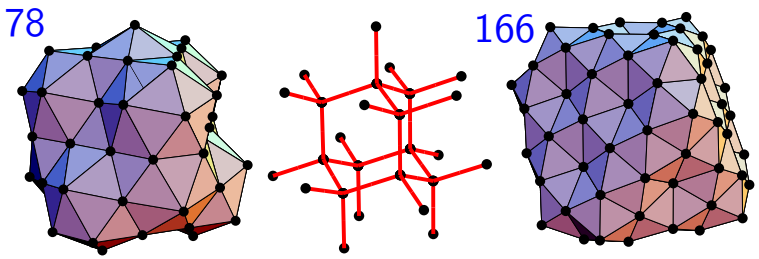

polytetrahedral clusters

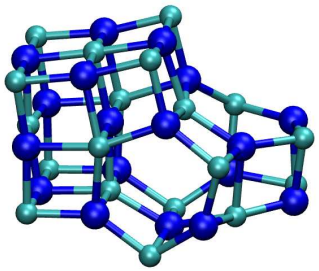

$(NaCl)_{18}Na^+$

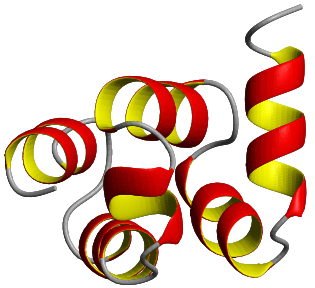

HYPA/FBP11

The Thomson Problem[28, 29]

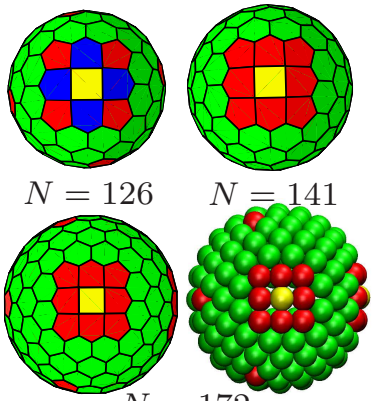

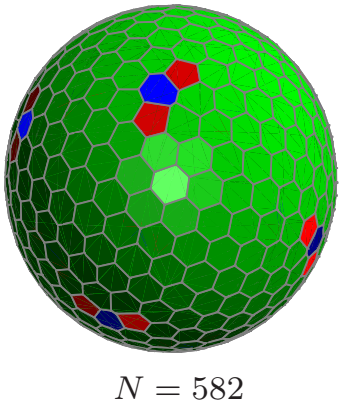

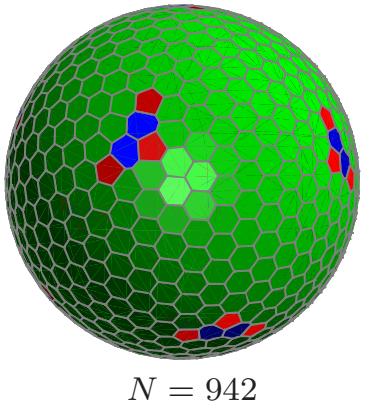

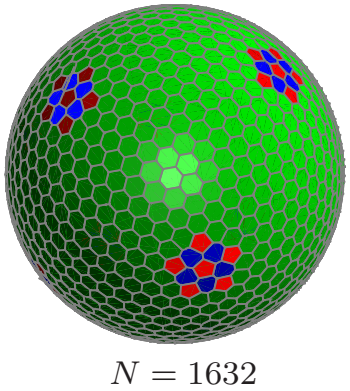

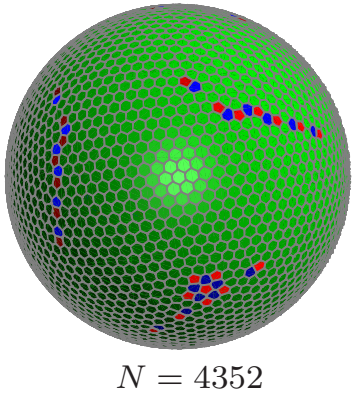

Long-ranged potential: $V = \sum_{i<j} 1/|\mathbf{r}_i - \mathbf{r}_j|$ with $|\mathbf{r}_i| = 1$. Twelve five-coordinate particles (disclinations) enable a spherical system to obey Euler's rule for the disclination charge.

Pentagon patches, extended dislocations (scars), twinned defects, rosettes, and embryonic grain boundaries occur in larger systems.

Structures provide models for spherically constrained systems: multielectron bubbles in superfluid helium, cell surface layers, 'colloidosomes', colloidal silica microspheres, superconducting films, lipid rafts deposited on vesicles.

Modelling Mesoscopic Structures

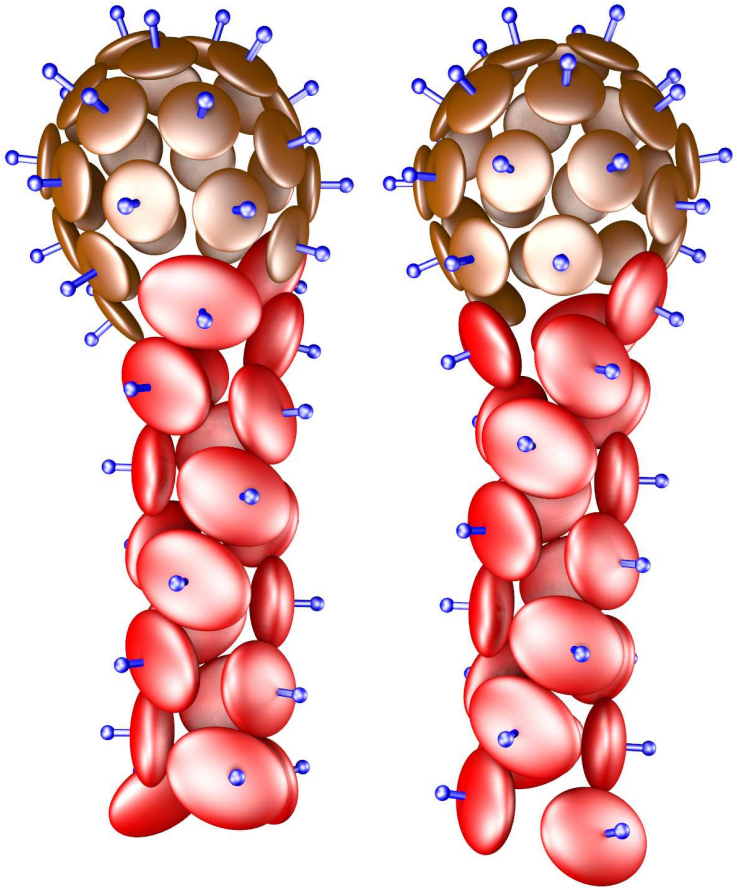

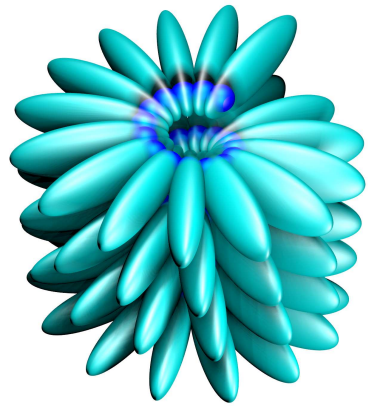

side

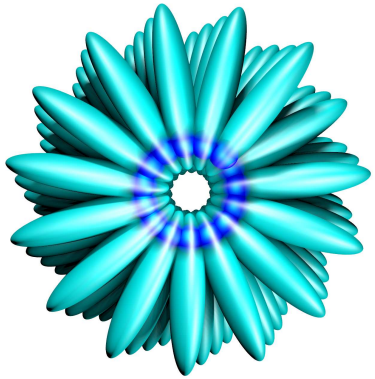

top

Mixing building blocks that favour shells and tubes produces structures with distinct head and tail regions (left): the **Frankenphage**.

Particles with a Lennard-Jones site buried in the ellipsoid assemble into a spiral structure (right) with parameters similar to tobacco mosaic virus.

Polytetrahedral Clusters

(a)

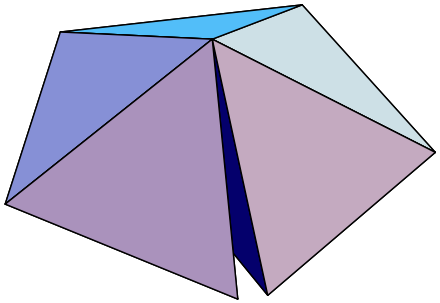

(b)

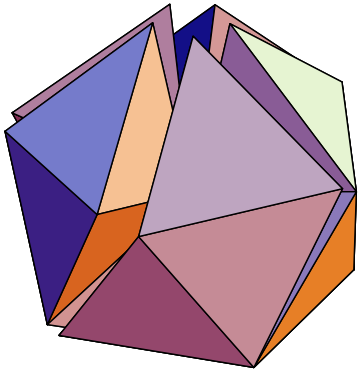

(c)

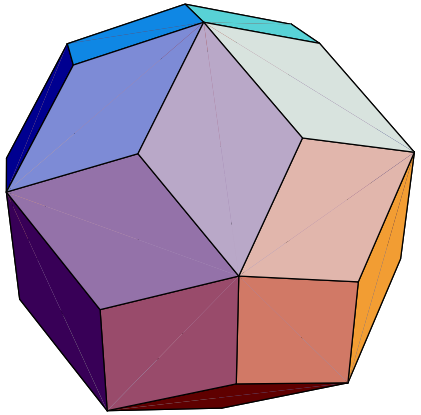

(a) Packing five regular tetrahedra around an edge leaves a gap of 7.36°.

(b) Packing twelve regular tetrahedra around a common vertex leaves a gap of 1.54 steradians.

Extended polytetrahedral packing requires negative disclination lines, where six tetrahedra share a common edge.

(c) For atomic clusters larger than the 45-atom rhombic triacontahedron (first described by Kepler) further polytetrahedral growth must involve disclinations.

Polytetrahedral packing is also found in quasicrystals, liquids and glasses.

For clusters Kasper polyhedra can be low-lying or global minima for interatomic potentials that enable strain to be accommodated.

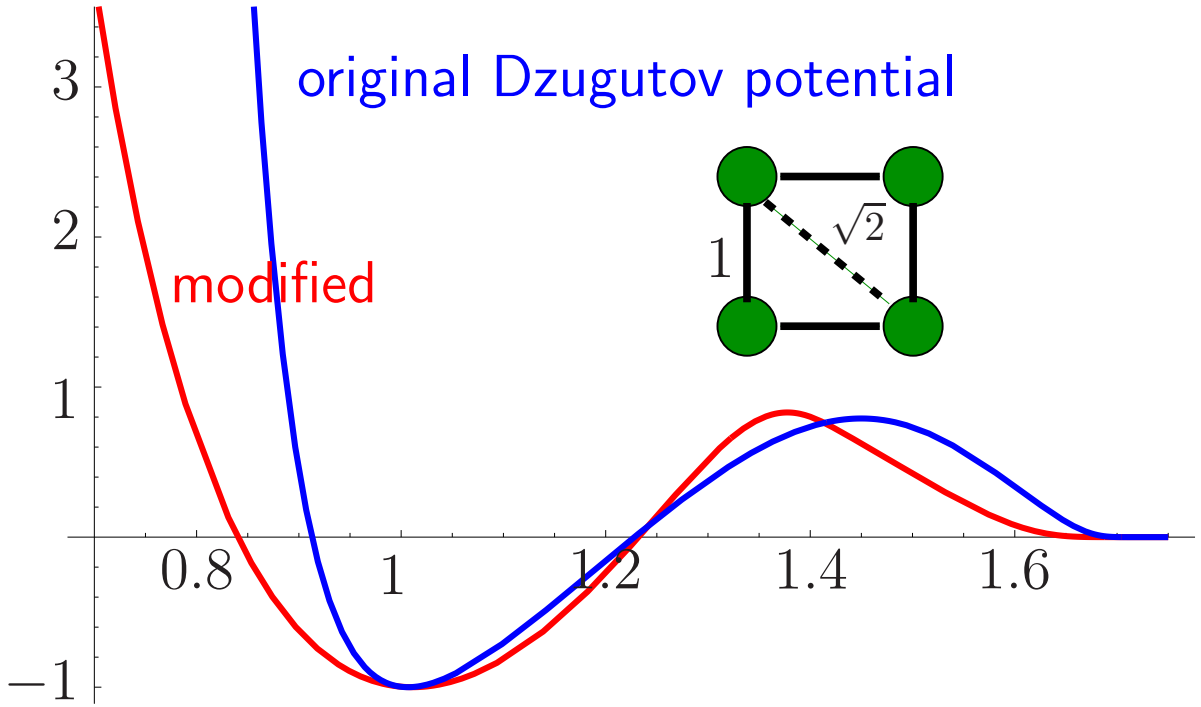

Dzugutov designed a potential (blue) to encourage polytetrahedral and local icosahedral order. This potential reproduces the structure of liquid MgZn, which forms a Frank-Kasper C14 solid phase.

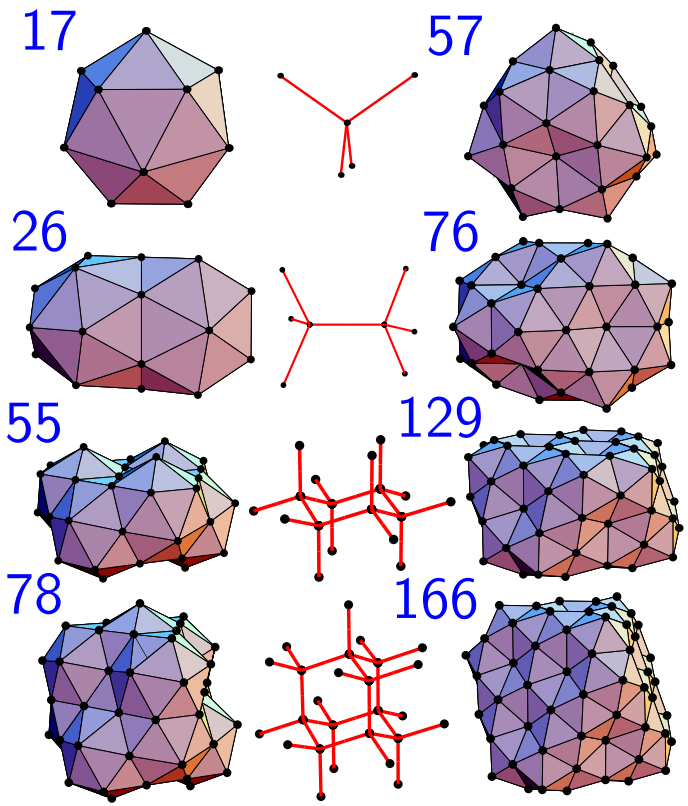

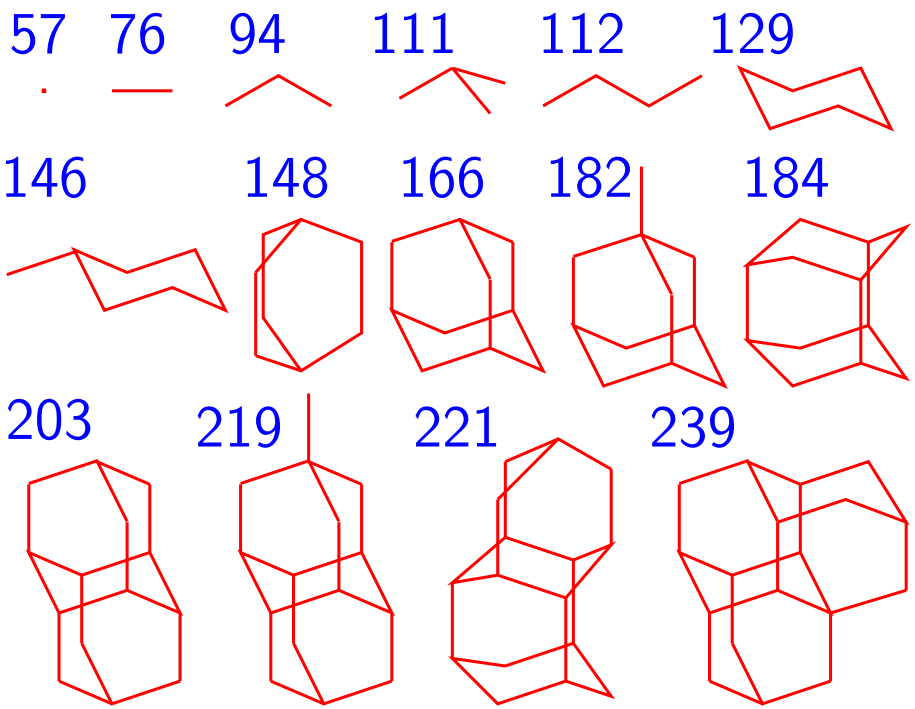

The disclination networks for the magic number clusters with the modified potential are analogous to linear, ring and cage hydrocarbon structures.

The calculated scattering function for the 166-atom adamantane analogue reproduces many of the features observed for cobalt clusters.

§5 Thermodynamics: the Superposition Approach

The harmonic approximation for the total energy density of vibrational states associated with a single minimum of a system with fixed centre of mass and fixed orientation with respect to space fixed axes gives[1]

$$\Omega(E) = \frac{(E - V^0)^{\kappa-1}}{\Gamma(\kappa) \prod_{j=1}^{\kappa} \nu_j}. \tag{4}$$

A factor of $1/h^\kappa$ provides the semiclassical approximation.

To calculate the total vibrational density of states all the minima need to be considered. In the superposition approximation we simply sum the density of states over all the minima low enough in energy to contribute.

This approximation is equivalent to assuming that the phase space hyperellipsoids associated with each minimum do not overlap.

$$\Omega(E) = \sum_{V_s^0 < E} \frac{n_s (E - V_s^0)^{\kappa - 1}}{\Gamma(\kappa) \prod_{j=1}^{\kappa} h\nu_j^s}, \tag{5}$$

where the sum is over all the structurally distinct minima on the surface and n_s, the number of permutational isomers of minimum s, is given by $n_s = 2N!/o_s$ where o_s is the order of the point group of s.

The canonical partition function in the same approximation is

$$Q(T) \;=\; \int \Omega(E) e^{-E\beta} dE \;=\; \sum_s \frac{n_s e^{-V_s^0 \beta}}{(\beta\, h\, \overline{\nu}_s)^{\kappa}}, \tag{6}$$

where $\beta = 1/kT$ and $\overline{\nu}_s$ is the geometric mean normal mode frequency.

The difficulty with equation (5) is that for all but the very smallest clusters the sum involves an impractically large number of minima.

Various reweighting schemes have been used to obtain an approximate global partition function based on local minima.

The basin-sampling approach[30] involves a convolution of the potential energy density of minima with vibrational densities of states.

Both basin-hopping global optimisation and basin-sampling require only local minimisation. In the reaction path Hamiltonian superposition approach (RPHSA) we use pathway information to improve the global partition function.[31]

Free energy surfaces for alanine dipeptide (CHARMM22/vacuum) from superposition, replica exchange, and RPHSA:

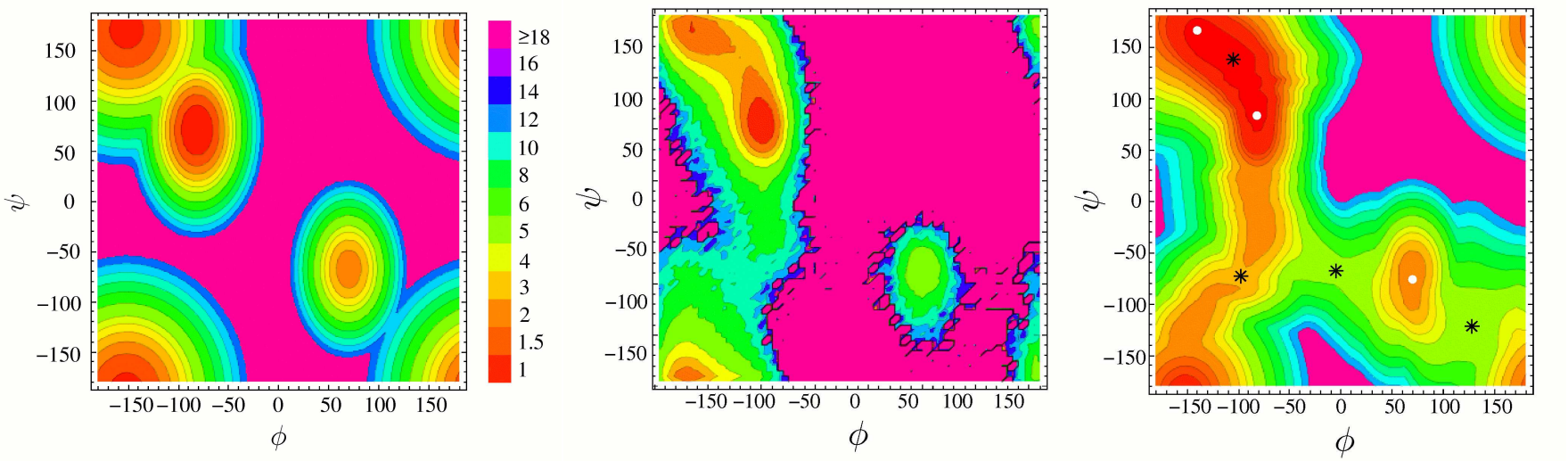

§5.1 The Reaction Path Hamiltonian Superposition Approach

The total partition function as a function of order parameter a is constructed as a superposition of contributions from local minima, $Z_i(a,T)$, and configurations taken from the pathways that connect them, $Z_r^\dagger(a,T)$:

$$Z_i(a,T) = \left(\frac{kT}{h\overline{\nu}_i}\right)^\kappa \frac{\exp\left(-V_i/kT\right)}{\sqrt{2\pi kTA_i}} \exp\left[-\frac{(a-a_i)^2}{2kTA_i}\right],$$

$$Z_r^\dagger(a,T) = \left(\frac{kT}{h}\right)^\kappa \frac{\delta_r \exp\left(-V_r^\dagger/kT\right)}{\left(\overline{\nu}_r^\dagger\right)^{\kappa-1} 2\pi kT\sqrt{A_r^\dagger}} \exp\left[-\frac{\left(a-a_r^\dagger\right)^2}{2kTA_r^\dagger}\right],$$

where $\overline{\nu}_i$ is the geometric mean of the normal mode frequencies, $\nu_{i,\gamma}$, V_i and a_i are the potential energy and order parameter for minimum i, $\kappa = 3N-6$, δ_r is a displacement, $\dagger$ labels transition states, and

$$A_i = \sum_{\gamma=1}^{\kappa} \left[\left.\frac{\partial a(\mathbf{q}_i)}{\partial q_{i,\gamma}}\right|_{\mathbf{q}_i=\mathbf{0}} \frac{1}{2\pi\nu_{i,\gamma}}\right]^2.$$

The method can be extended for projections onto additional order parameters.

The 'filling in' problem for barrier regions in low-dimensional projections due to overlapping distributions can be avoided using disconnectivity graphs.

The effect of regrouping for a barrier threshold of 3 kcal/mol is shown below for AMBER(ff03)/GB$^{\mathrm{OCB}}$ (left) and compared with the CHARMM22/vacuum surface (right). Free energy of group J: $F_J(T) = -kT \ln \sum_{j \in J} Z_j(T)$ with

$$F^{\dagger}_{LJ}(T) = -kT \ln \sum_{l \leftarrow j} Z^{\dagger}_{lj}(T), \quad \text{and} \quad k_{LJ}(T) = \frac{kT}{h} e^{-\left[F^{\dagger}_{LJ}(T) - F_J(T)\right]/kT}.$$

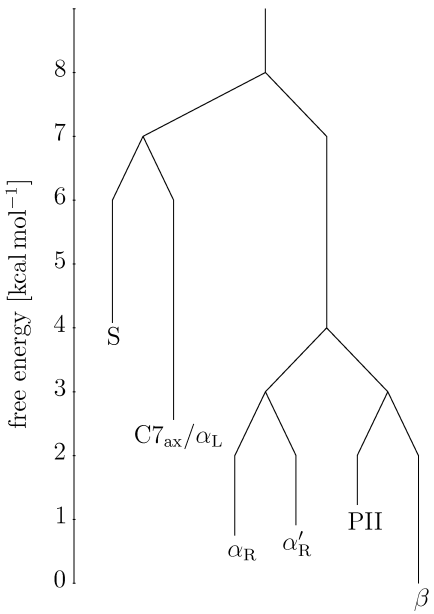

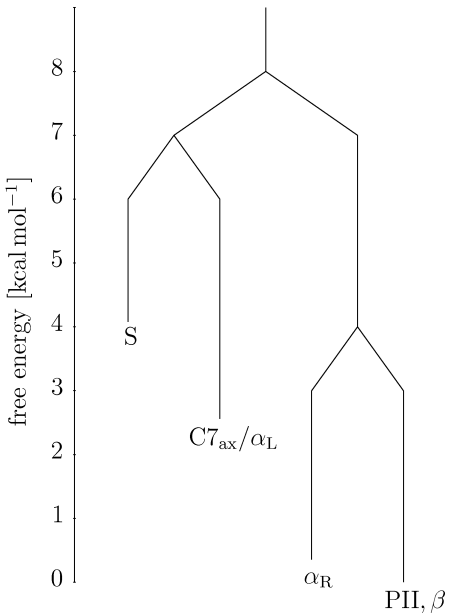

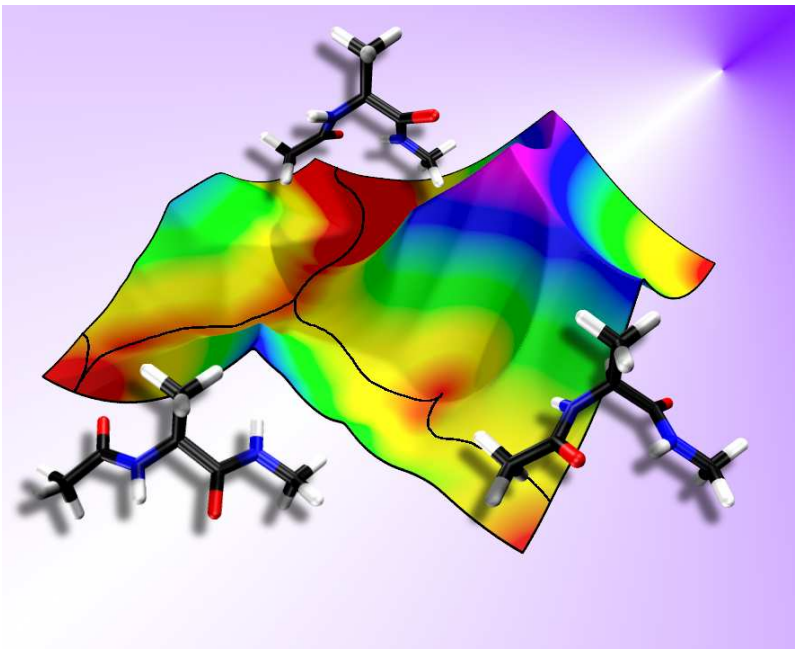

§6 Global Dynamics

A database of local minima and the transition states that connect them constitutes a kinetic transition network.[31,32]

To complete this coarse-grained representation we need the rate constants associated with the forward and backward rates for each transition state.

If the minimum-to-minimum dynamics are assumed Markovian then the time evolution of the occupation probabilities $\mathbf{P}(t) = (P_1(t), P_2(t), \ldots)^T$ is described by a 'master equation':

$$\frac{dP_{\mathrm{a}}(t)}{dt} = \sum_{\mathrm{b}\neq\mathrm{a}} [k_{\mathrm{ab}} P_{\mathrm{b}}(t) - k_{\mathrm{ba}} P_{\mathrm{a}}(t)], \tag{7}$$

where $P_{\mathrm{a}}(t)$ is the probability of the system being in state a at time t, and k_{ab} is the rate constant for transitions from minimum b to minimum a.

Consistent theories must be used for thermodynamic properties, such as P^{eq}, and the rate constants, so that detailed balance is satisfied.

The transition state theory expression for the unimolecular canonical rate constant $k_{\mathrm{a}}^{\dagger}$, out of minimum a through transition state $\dagger$ is

$$k_{\mathrm{a}}^{\dagger}(T) = \frac{kT}{h}\frac{Z^{\dagger}}{Z_{\mathrm{a}}}\mathrm{e}^{-\Delta V/kT}, \tag{8}$$

where the transition state partition function $Z^{\dagger}$ does not include the unique mode with imaginary frequency, and $\Delta V = V^{\dagger} - V_a$ is the potential energy difference between the transition state and minimum a.

Using harmonic vibrational densities of states gives:

$$k_{\mathrm{a}}^{\dagger}(T) = \frac{\bar{\nu}_{\mathrm{a}}^{\kappa}}{\bar{\nu}^{\dagger(\kappa-1)}}\mathrm{e}^{-(V^{\dagger}-V_{\mathrm{a}})/kT}. \tag{9}$$

In this picture all minimum-to-minimum transitions are activated, in the sense that there is an underlying barrier on the PES.

The rearrangement barriers involved in diffusion and structural relaxation are intensive quantities. Rate constants depend only on ratios of either intensive or extensive quantities,[15,16] independent of system size.

In defining a transition state as a stationary point with a single negative Hessian eigenvalue we follow the geometrical approach of Murrell and Laidler.[33]

There are two reasons why these points provide the foundation for a coarse-grained formulation of global kinetics.

The Murrell-Laidler theorem states that *if two local minima are connected by a path involving a saddle point of index two or more, then a lower energy path exists involving only true transition states with index one*.

Proof: consider a saddle point with two negative Hessian eigenvalues, ω_1^2 and ω_2^2, for normal modes Q_1 and Q_2. With all the other coordinates fixed the change in potential energy, $\Delta\mathcal{V}$, for small displacements from the saddle is:

$$\Delta\mathcal{V} = \frac{1}{2}(\omega_1^2\, Q_1^2 + \omega_2^2\, Q_2^2) < 0. \tag{10}$$

Hence any displacement in this two-dimensional space lowers the energy. The saddle is therefore a 'hill' in these two dimensions.

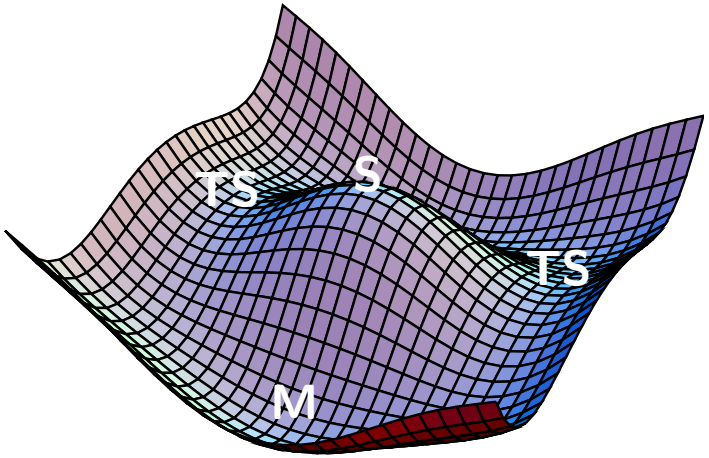

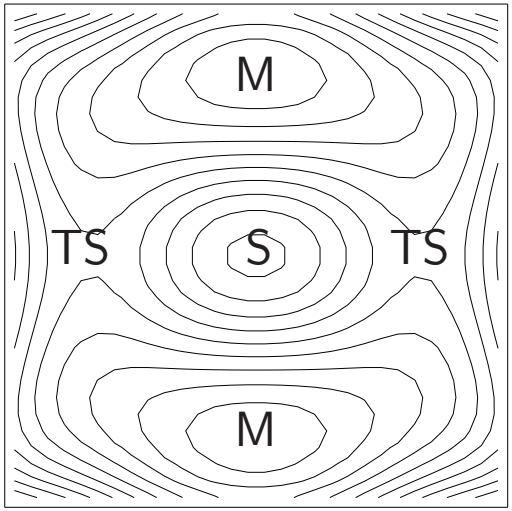

Surface and contour plots illustrating the Murrell-Laidler theorem. M, TS and S denote minima, transition states and the index two saddle, respectively.

To derive the transition state theory rate constant we define a dividing surface between reactants and products, and assume no dynamical recrossings.[34, 35]

The eigenvector corresponding to the unique negative Hessian eigenvalue of an index one saddle defines a hyperplane, which acts as the dividing surface in a local harmonic expansion about the transition state.

Higher index saddles are not required in unimolecular rate theory.

§6.1 Discrete Path Sampling[36,37]

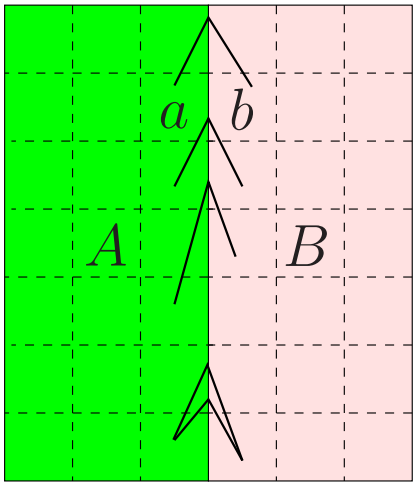

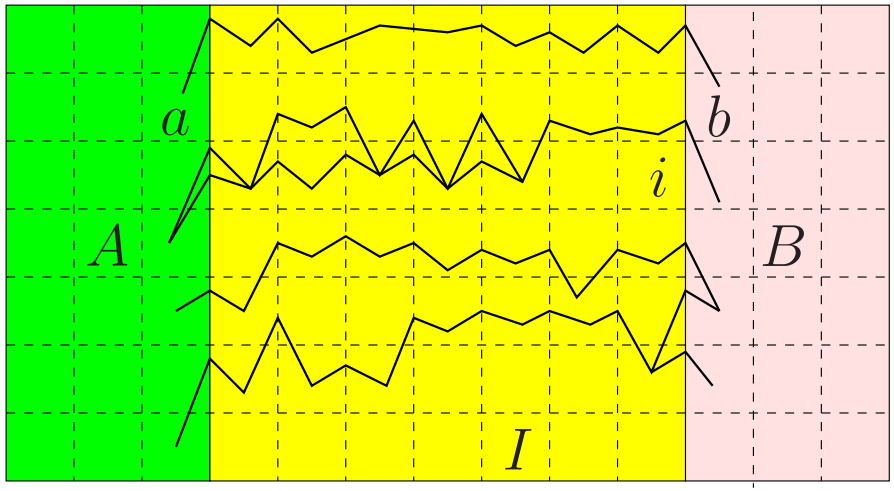

no intervening minima $\frac{p_a(t)}{p_{a'}(t)} = \frac{p_a^{\rm eq}}{p_{a'}^{\rm eq}}$ $\dot{p}_i(t) = 0$ $\frac{p_b(t)}{p_{b'}(t)} = \frac{p_b^{\rm eq}}{p_{b'}^{\rm eq}}$

Phenomenological $A \leftrightarrow B$ rate constants can be formulated as sums over discrete paths, defined as sequences of local minima and the transition states that link them, weighted by equilibrium occupation probabilities, $p_b^{\rm eq}$:

$$k_{AB}^{\rm SS} = \frac{1}{p_B^{\rm eq}} \sum_{a \leftarrow b} P_{ai_1} P_{i_1 i_2} \cdots P_{i_{n-1} i_n} P_{i_n b} \tau_b^{-1} p_b^{\rm eq} = \frac{1}{p_B^{\rm eq}} \sum_{b \in B} \frac{C_b^A p_b^{\rm eq}}{\tau_b},$$

where $P_{\alpha\beta}$ is a branching probability and C_b^A is the committor probability that the system will visit an A minimum before it returns to the B region.

§6.2 Permutational Isomerisation of LJ_7^{2D}

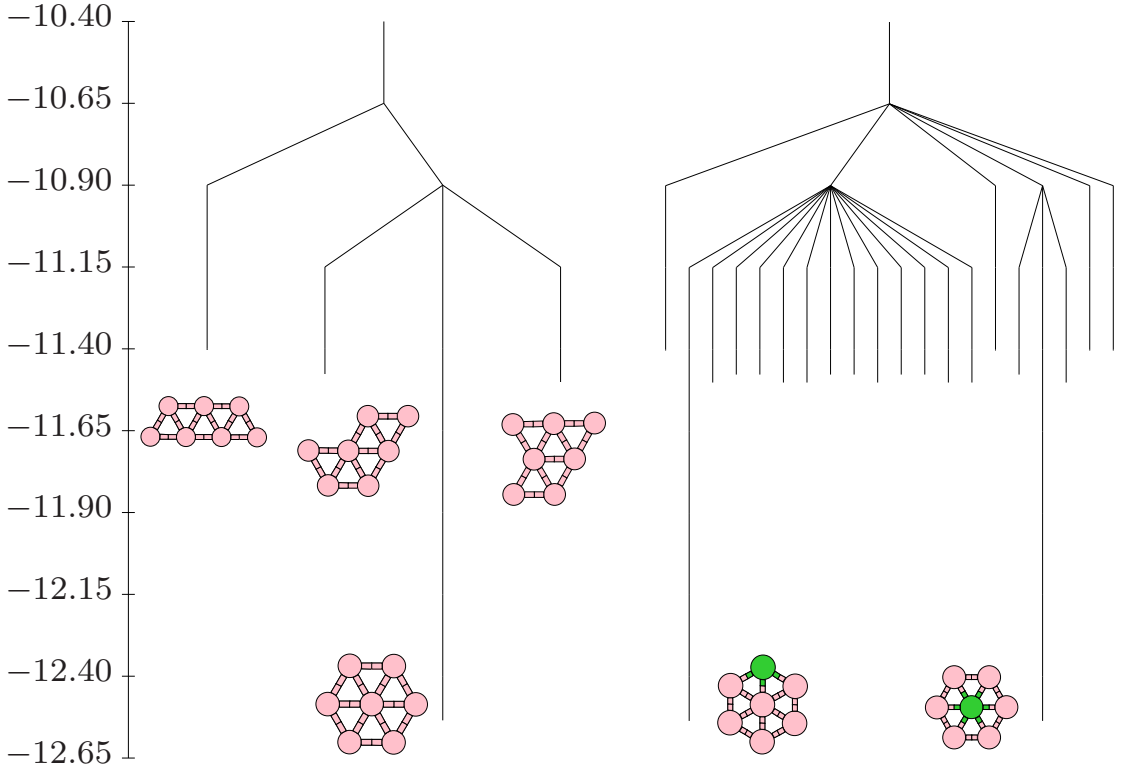

Disconnectivity graphs for LJ_7^{2D}. Left: permutation-inversion isomers of the four local minima are collected together. Right: one of the atoms is tagged, lowering the permutational degeneracy.

The fastest ten paths contribute about 74% of the total rate constant at $kT/\epsilon = 0.05$. Various combinations of diamond-square-diamond rearrangements make significant contributions.

§7 Bulk Matter

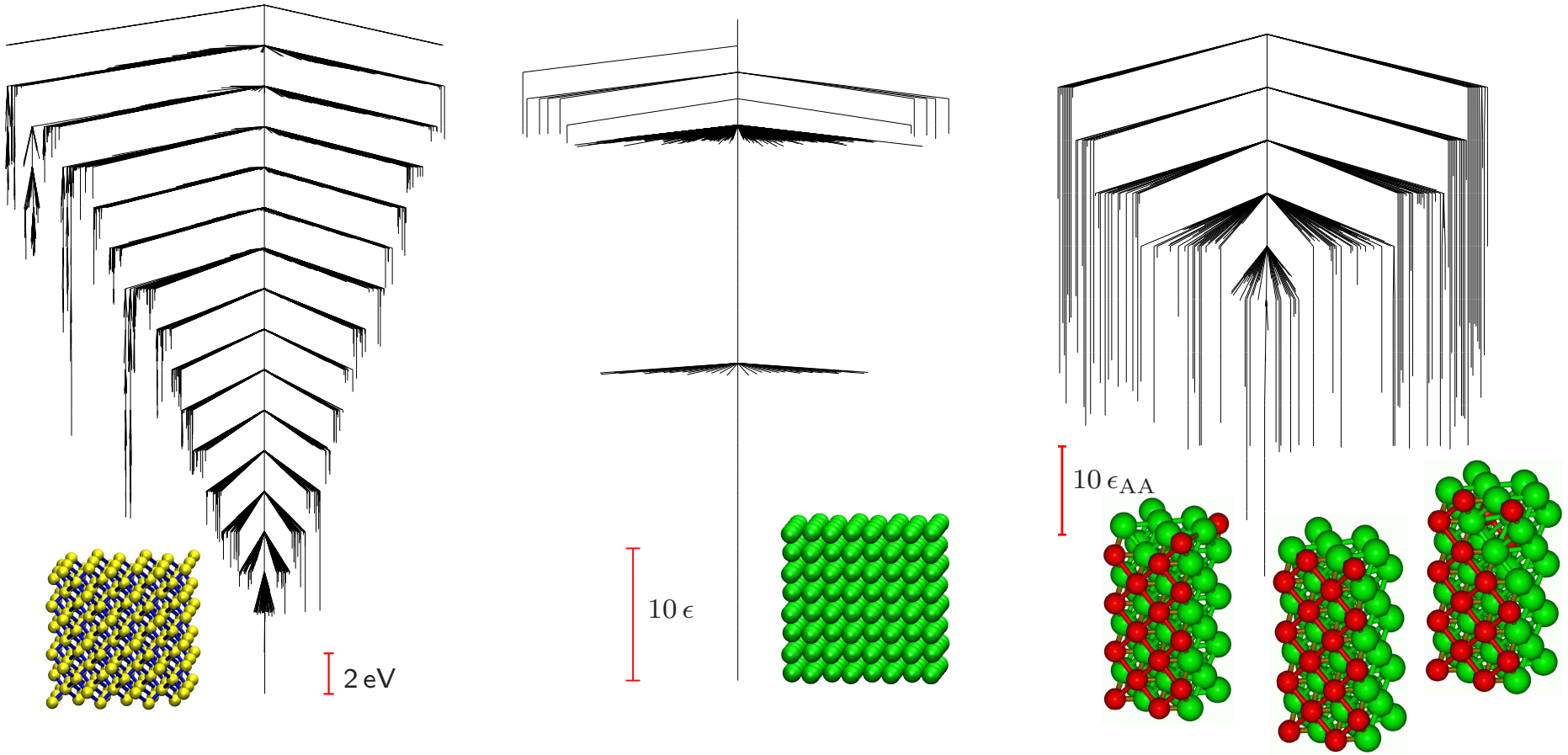

Disconnectivity graphs in the vicinity of the crystal for Stillinger-Weber silicon (left), a Lennard-Jones solid (middle), and a binary Lennard-Jones (BLJ) model (right). The BLJ landscape is clearly more frustrated, with larger downhill barriers to the perfect crystal.

§7.1 Thermodynamics of the BLJ Solid[38]

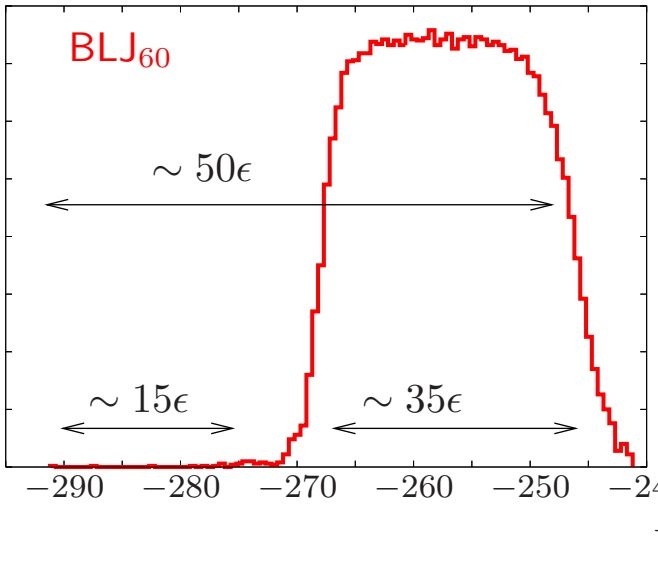

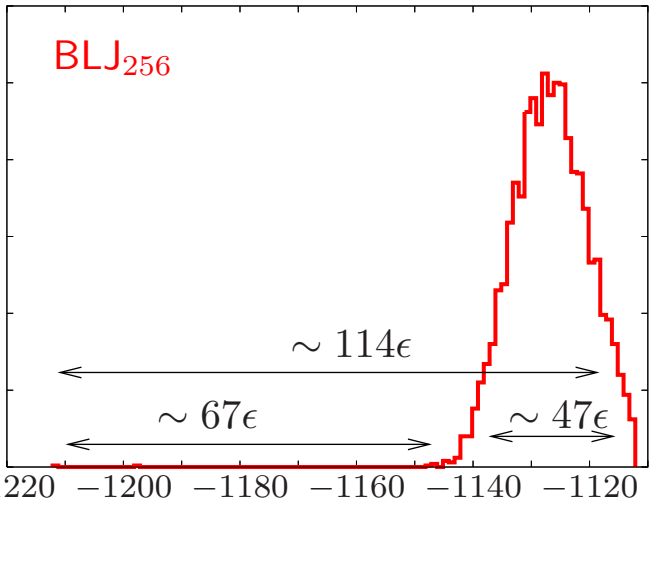

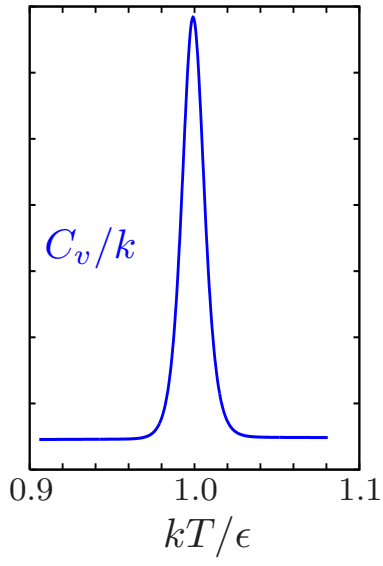

Equilibrium thermodynamic properties such as $\Omega(E)$ and C_v (right, for BLJ_{320}) can be obtained from parallel tempering, despite the extensive energy gap in the probability distribution for local minima between the crystal and the amorphous states (left).

We were unable to converge Wang-Landau calculations because the probability of return to the crystal from the amorphous region is so low, even when a two-dimensional scheme based on $\Omega(E, Q_6)$ was used.

§7.2 Glassy Phenomenology[39]

To calculate the thermodynamic and kinetic properties of supercooled liquids and glasses using coarse-grained descriptions based on stationary points we must allow for ergodicity breaking.[39–41]

Acknowledging that ergodicity can be associated with an observation time scale,[42] τ, we should write a superposition partition function that includes only the accessible configuration space:[39]

$$Z(T,\tau) = Z_x(T)\Theta[f_x(T) - 1/\tau] + \sum_{a=1} Z_a(T)\Theta[f_a(T) - 1/\tau]. \qquad (11)$$

Here, Θ is the Heaviside step function, the sum is over regions of the PES a, $f_a(T)$ is the probability flux out of region a at temperature T, and region x corresponds to the crystal.

f_a is also a function of τ because the flux depends upon which regions are connected.

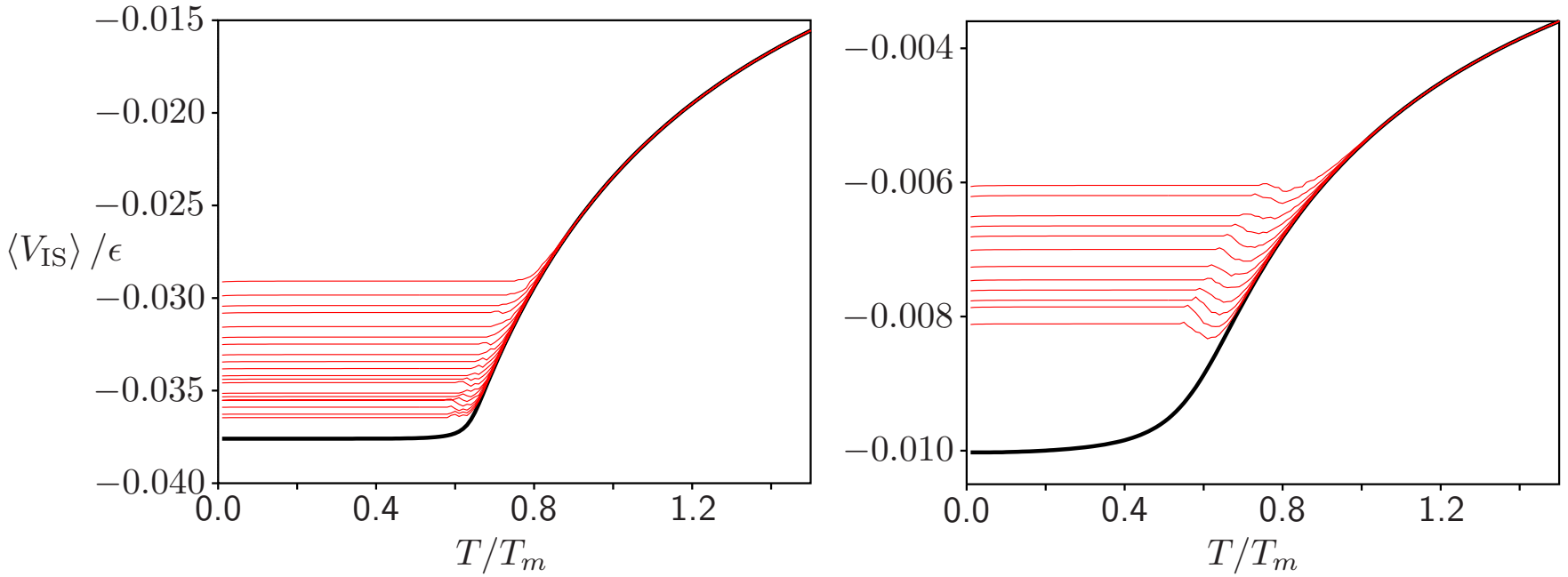

Average potential energy of the occupied minima as a function of temperature and observation time scale for a model PES.[39]

$\langle V_{\mathrm{IS}} \rangle$ is a function of both T and τ. The red lines correspond to increasing τ for decreasing potential energy, and the solid black line is the result corresponding to equilibrium within the non-crystalline phase space.

The left and right panels correspond to parameter sets that produce fragile and strong behaviour, respectively.

Longer observation times, corresponding to slower cooling rates, result in relaxation to deeper potential energy minima, as expected.[43]

For an infinite time scale, but excluding the crystal, i.e. equilibrium within the non-crystalline configuration space, the model exhibits an underlying second-order phase transition.[39]

Fragility is associated with more local minima, lower effective potential energy barriers, and higher vibrational frequencies, in agreement with Angell's previous suggestions.[44]

Increasing the energy density of minima alone was found to produce more fragile thermodynamics but stronger, more Arrhenius, dynamics.

However, systems with a higher density of local minima are expected to have higher vibrational frequencies, and the observed correlations between dynamic and thermodynamic properties for strong and fragile behaviour are then recovered.[39]

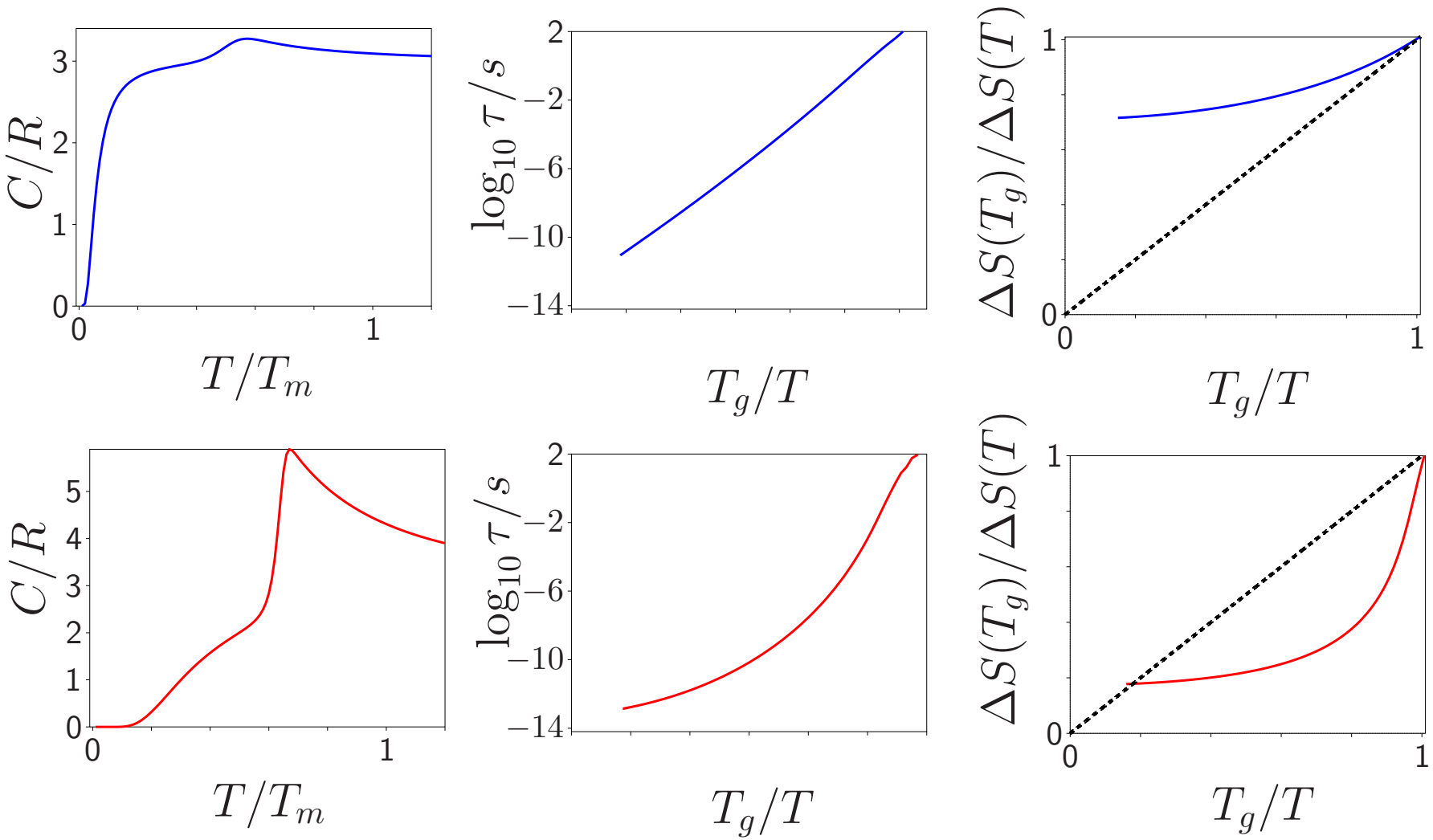

The heat capacity, C, relaxation time, τ, and entropy difference, $\Delta S = S_{\text{liquid}} - S_{\text{crystal}}$, of strong and fragile liquids calculated within this model are compared above.

§7.3 Glassy Landscapes

Barrier distributions for bulk models have been reported using both eigenvector-following[45–47] and the activation-relaxation approach,[48–51] including enthalpy barriers at constant pressure.[47,52]

The barrier heights for cage-breaking processes are significantly larger than for non-cage-breaking processes, and the difference is greater for silicon (Stillinger-Weber potential) than for BLJ.[46]

The barriers that we deduce from the slope of an Arrhenius plot for the diffusion constant or the viscosity correspond to multiple transition states on the potential energy or enthalpy surface.

The large number of rearrangements with low barriers indicates that the system is not trapped in a single local minimum at the glass transition.[15,39,46,47]

Sets of minima that can interconvert without encountering a cage-breaking rearrangement[53–55] may provide a useful definition of a 'metabasin'.[56]

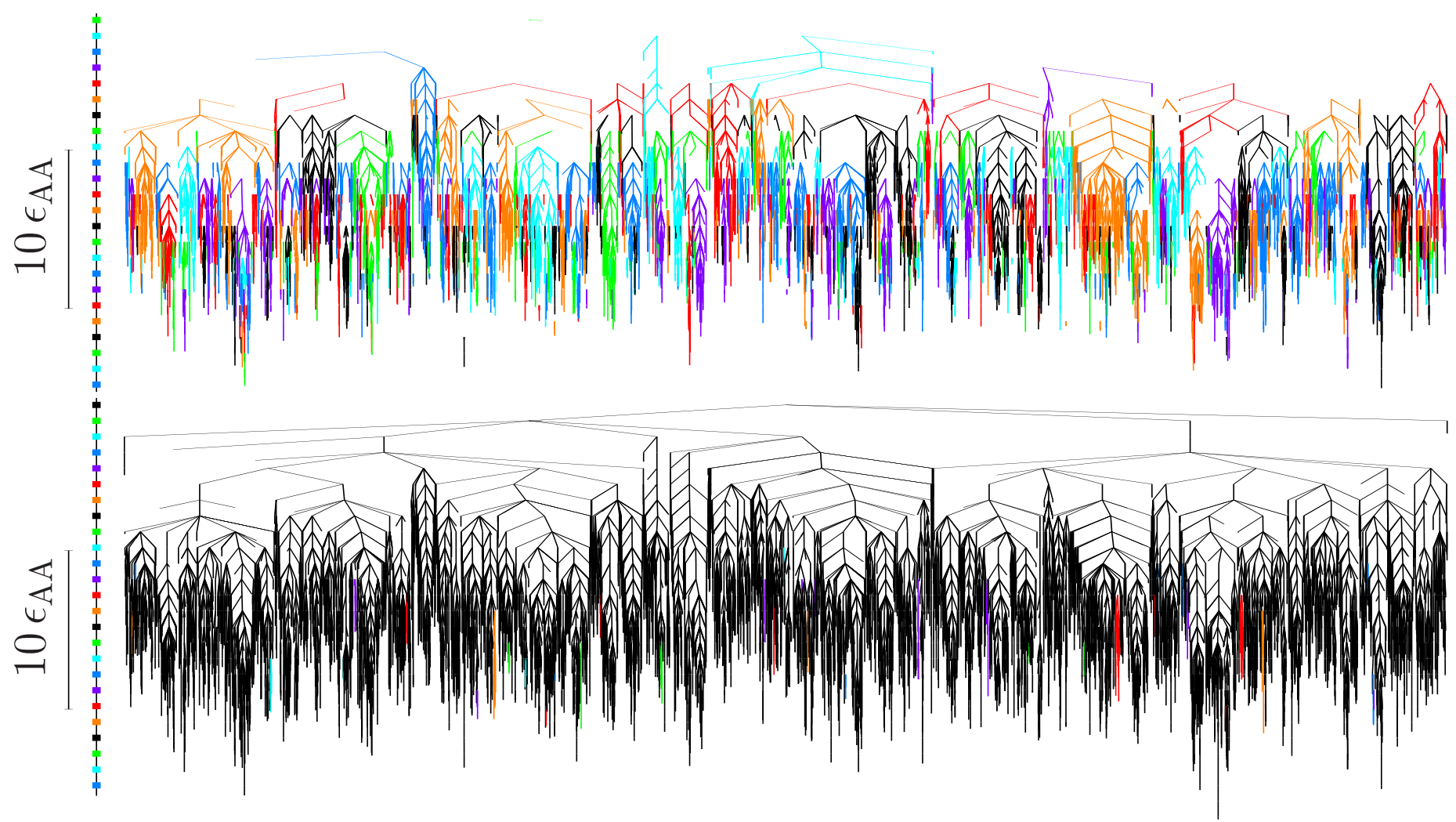

Disconnectivity graphs for BLJ_{60} including only transition states for noncage-breaking (top) and cage-breaking (bottom) paths.[56] Changes in colour indicate disjoint sets of minima. Cage-breaking transitions, defined by two nearest-neighbour changes, define a higher order metabasin structure.

§7.4 Strong and Fragile Dynamics for the BLJ Solid

To identify local ergodicity in a molecular dynamics trajectory we have used the energy fluctuation metric of Mountain and Thirumalai,[57] defined in terms of the time-averaged energy of the jth particle of type α, $\epsilon_j(t;\alpha)$, as

$$\Gamma(t) = \sum_{\alpha} \frac{1}{N} \sum_{j=1}^{N_\alpha} [\epsilon_j(t;\alpha) - \overline{\epsilon}(t;\alpha)]^2, \tag{12}$$

$$\text{where} \quad \overline{\epsilon}(t;\alpha) = \frac{1}{N_\alpha} \sum_{j=1}^{N_\alpha} \epsilon_j(t;\alpha). \tag{13}$$

If the system is ergodic within a well-defined region of configuration space, $\Gamma(t)$ should vanish for long times, as the average energy of each individual particle reaches the ensemble average for the appropriate species, α.

For a particular trajectory, the form of $\Gamma(t)$ plotted against $1/t$ can be used to determine ergodic and non-ergodic time scales.[58,59]

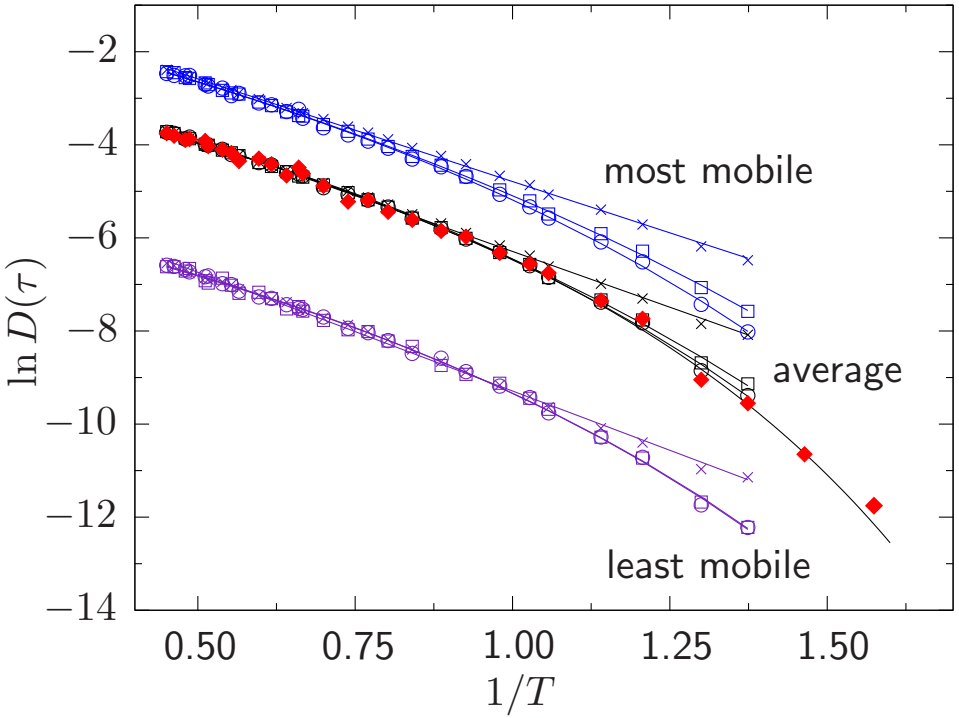

We calculate $D(\tau)$ by dividing a locally ergodic trajectory into shorter segments. The figure shows results for the most and least mobile A atoms, along with the average, for $\tau = 25,\ 250$ and 2500 (crosses, squares and circles) in a 60-atom BLJ mixture with number density 1.3.

The true diffusion constant obtained by averaging over all A atoms on the longest time scale is shown by filled diamonds.

On short non-ergodic time scales all the atoms, whether more or less mobile, exhibit Arrhenius behaviour.

The true super-Arrhenius behaviour at this density results from negative correlation between the atomic displacements in successive time windows, not from a distribution of barrier heights.

To quantify this correlation, we write the mean square displacement after time, t, in terms of atomic displacements in m time intervals of length τ,

$$\begin{aligned}\Delta\mathbf{r}_i(t)^2 &= \sum_{j=1}^{m} \Delta\mathbf{r}_i(j)^2 + 2\sum_{j<k} \Delta\mathbf{r}_i(j)\cdot\Delta\mathbf{r}_i(k) \\ &= \sum_{j=1}^{m} \Delta\mathbf{r}_i(j)^2 + 2\sum_{j<k} |\Delta\mathbf{r}_i(j)||\Delta\mathbf{r}_i(k)|\cos\theta_{jk}. \qquad (14)\end{aligned}$$

When determining the mean square displacement for a time interval τ, we include the first term in Equation (14) but not the second term.

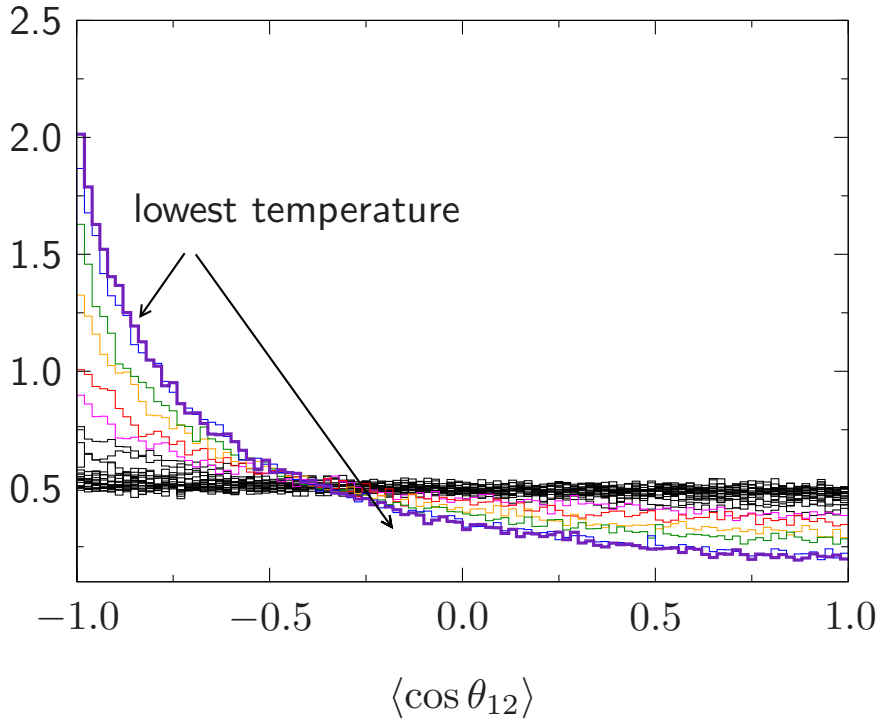

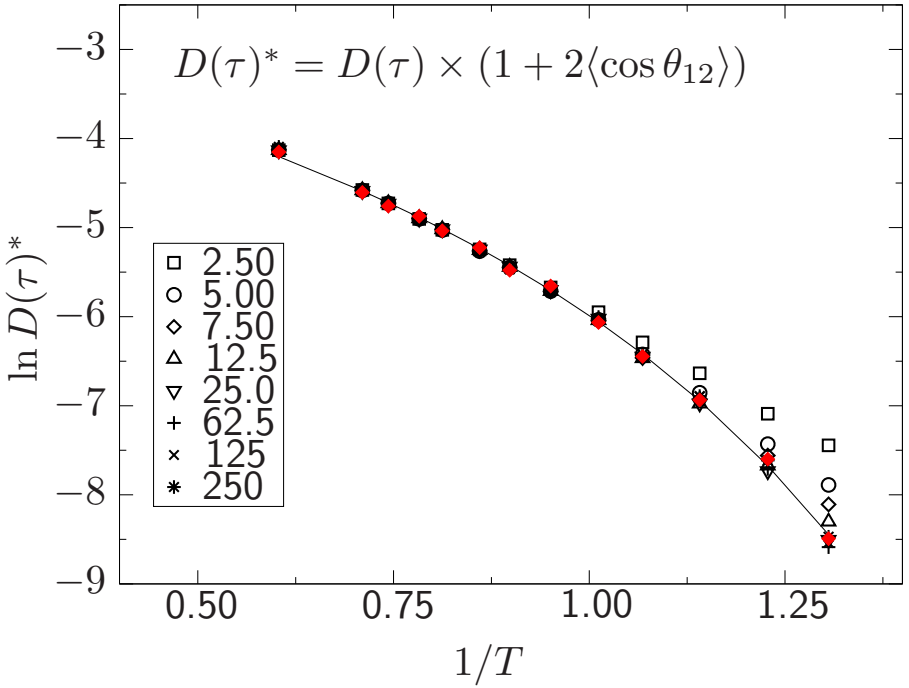

The behaviour of $D(\tau)$ shows that this second term is nonzero at low temperature, and by effectively averaging over the atoms too early, we miscalculate the diffusion constant and obtain Arrhenius temperature dependence.[59, 60]

The second term is therefore responsible for the super-Arrhenius behaviour.

Displacements within successive time windows are negatively correlated on average (left). $D(\tau)$ can be corrected as $D(\tau)^* = D(\tau) \times (1 + 2\langle \cos\theta_{12} \rangle)$.

To calculate the diffusion constant from local properties of the energy landscape we need to know the connectivity of a representative local minimum in terms of cage-breaking processes, and the probability that such cage-breaking events are not simply reversed.[61]

The number of reversals increases at lower temperatures and for more fragile systems, as the number of accessible connections decreases.

Cage-breaking events, which are necessary for diffusion, can be modelled as a correlated random walk, and for BLJ it is sufficient to consider short simulations that extend up to two cage-breaking events.

Instead of coarse-graining over time window steps, as above, we are now considering the correlations between cage-breaking events.

In this analysis fragility is associated with a larger entropic barrier, which results from a faster reduction in connectivity as the temperature decreases, and hence more cage-breaking reversals.[61]

§8 A Connection Between Dynamics and Thermodynamics[4]

The organisation of a PES is governed by its stationary points, where Taylor expansions provide local descriptions in terms of Hessian matrices.

The organisation of families of PES's as a function of parameters in the potential is determined by the stationary points that possess additional zero Hessian eigenvalues, known as non-Morse points.

Catastrophe theory provides a local representation of the PES around non-Morse points as a function of both atomic coordinates and parameters.

The splitting lemma reduces the dimensionality to the essential variables, while transversality guarantees that the resulting classifications are universal.

The simplest one-parameter catastrophes are the fold, $f(x) = \frac{1}{3}x^3 + ax$, and the symmetrical cusp, $f(x) = \frac{1}{4}x^4 + \frac{1}{2}ax^2$.

When $a = 0$ there is a non-Morse point where there is an additional zero Hessian eigenvalue. This point separates families of surfaces for $a < 0$ and $a > 0$ with different topologies.

We can eliminate parameters of the universal form in favour of ΔV, the energy difference between the transition state and the minimum, the curvature at the minimum, λ, and the displacement between the stationary points, Δs.

For the fold catastrophe we find $6\Delta V/\lambda(\Delta s)^2 = 1$, and the smallest Hessian eigenvalue of the transition state approaches $-\lambda$.

Similarly, for the symmetrical cusp $4\Delta V/\lambda(\Delta s)^2 = 1$.

The fold and cusp ratios, $r_{\mathrm{f}} = 6\Delta V/\lambda(\Delta s)^2$, and $r_{\mathrm{c}} = 4\Delta V/\lambda(\Delta s)^2$ should tend to unity in the limit of short path lengths for catastrophes of the corresponding form.

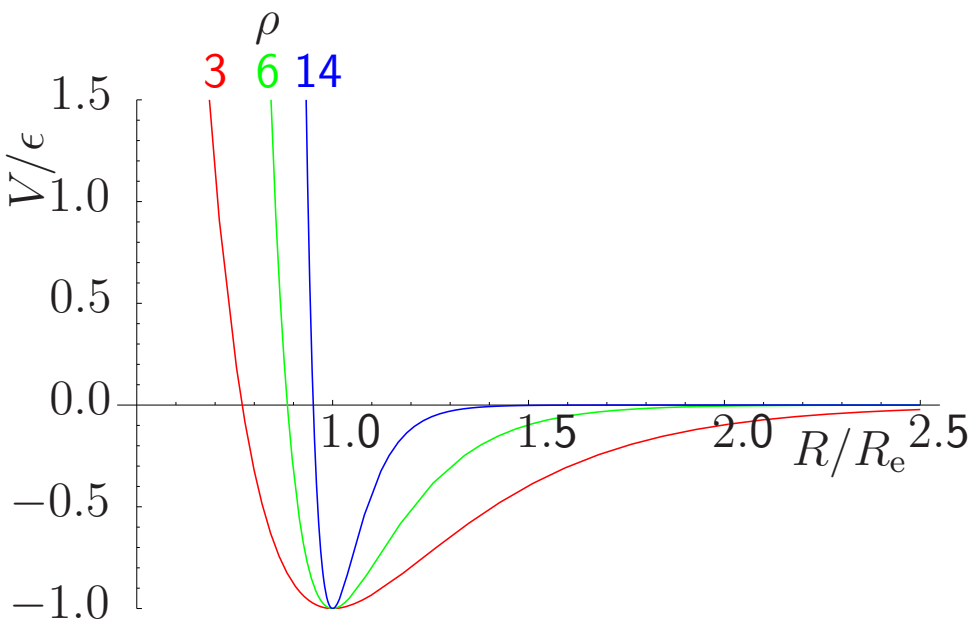

The Morse potential as a function of the distance between two atoms is:

$$V = \epsilon e^{\rho(1-R/R_{\rm e})}\left[e^{\rho(1-R/R_{\rm e})} - 2\right], \tag{15}$$

ϵ and $R_{\rm e}$ are the dimer well depth and equilibrium bond length. They can conveniently be set to unity and used as the units of energy and distance.

ρ is a dimensionless parameter that determines the range of the inter-particle forces, with low values corresponding to long range.

Physically meaningful values vary from $\rho \sim 3$ for sodium to around 14 for C_{60} molecules. When $\rho = 6$, the Morse potential has the same curvature as the Lennard-Jones potential at the minimum.

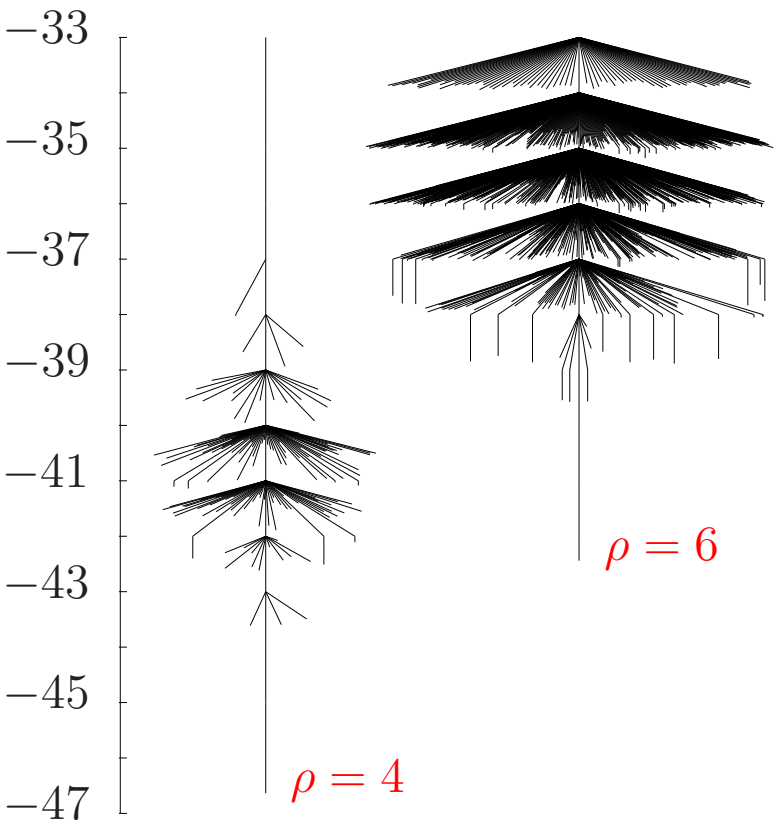

Disconnectivity graphs for M_{13} with $\rho = 4$ and $\rho = 6$ plotted on the same energy scale (in units of the pair well depth).

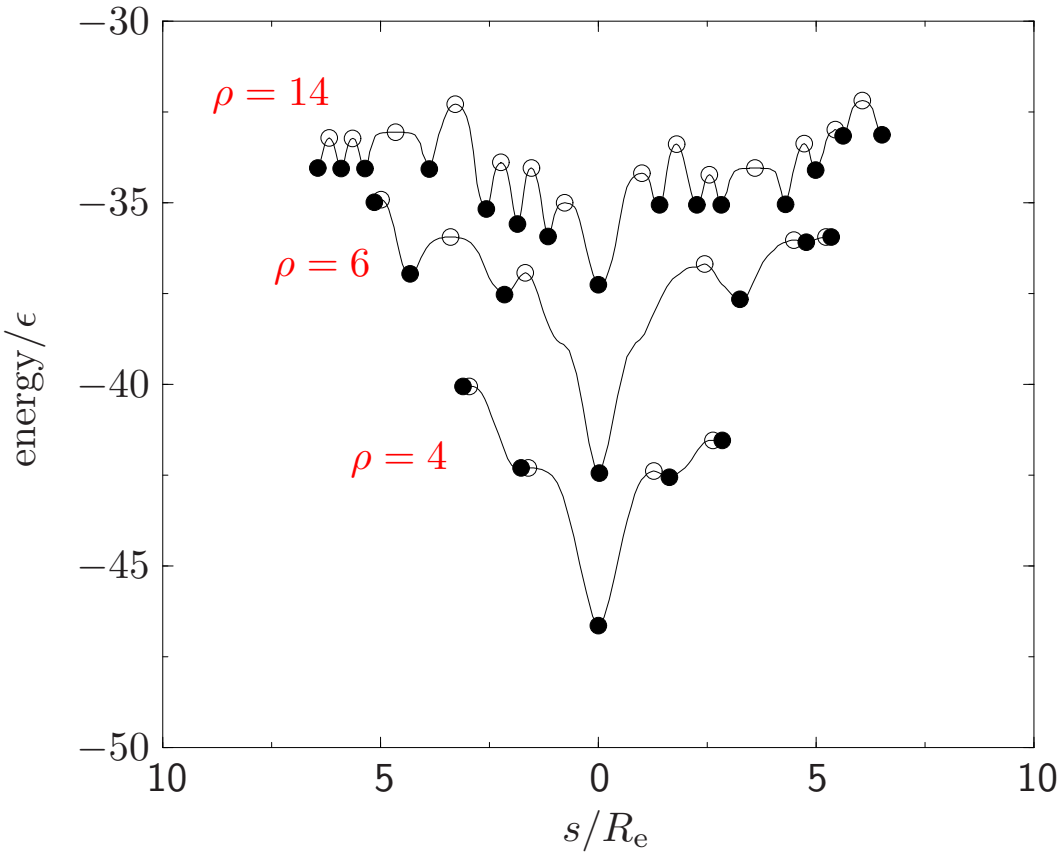

Short-ranged potentials lead to potential energy surfaces that are rougher but flatter. As the range increases minimum/transition state pairs are progressively eliminated as they merge together at non-Morse points corresponding to fold (or other) catastrophes.

Both ΔV and Δs tend to zero as a minimum and transition state approach, but ΔV must decrease faster than $(\Delta s)^2$ because the ratio is proportional to λ, which also tends to zero.

This trend on its own would tend to decrease both uphill and downhill barriers.

However, when a minimum disappears the steepest-descent paths that connected it to higher energy transition states must continue downhill to lower energy, and the corresponding barriers increase discontinuously.

Hence, as the curvature of the potential decreases the larger barriers and path lengths tend to grow, while smaller barriers and path lengths tend to shrink.

These results explain Hammond's postulate:[62] 'if two states, as for example a transition state and an unstable intermediate occur consecutively during a reaction process and have nearly the same energy content, their interconversion will involve only a small reorganisation of the molecular structures'.

Geometries of the fold and cusp catastrophes.

curvature$= -\lambda$

fold: $r_{\mathrm{f}} = \dfrac{6\Delta V}{\lambda \Delta s^2} = 1$

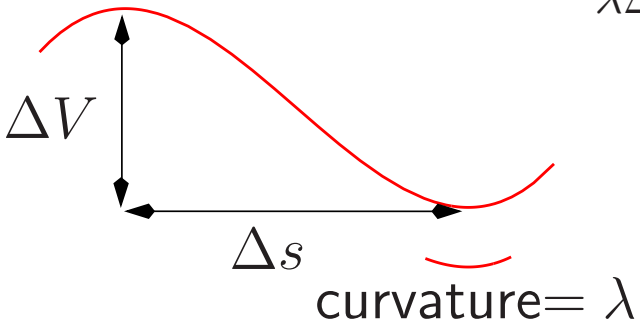

curvature$= \lambda$

curvature$= -2\lambda$

cusp: $r_{\mathrm{c}} = \dfrac{4\Delta V}{\lambda \Delta s^2} = 1$

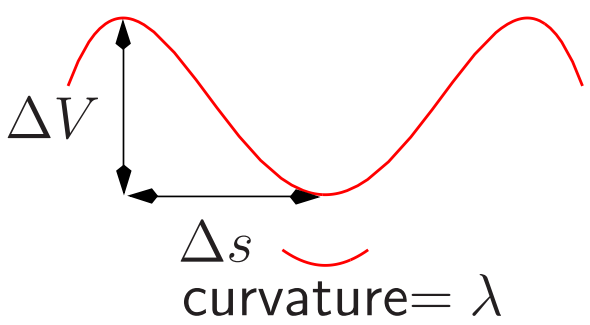

curvature$= \lambda$

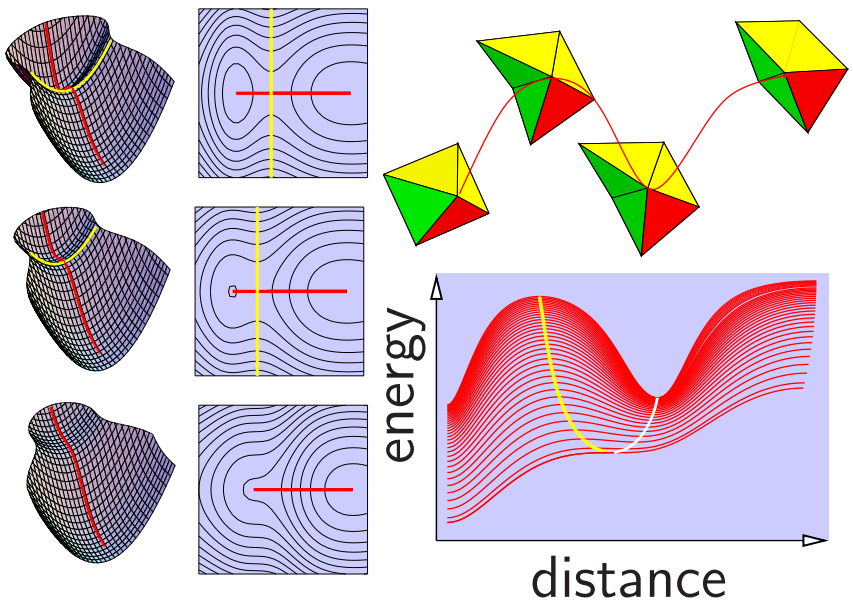

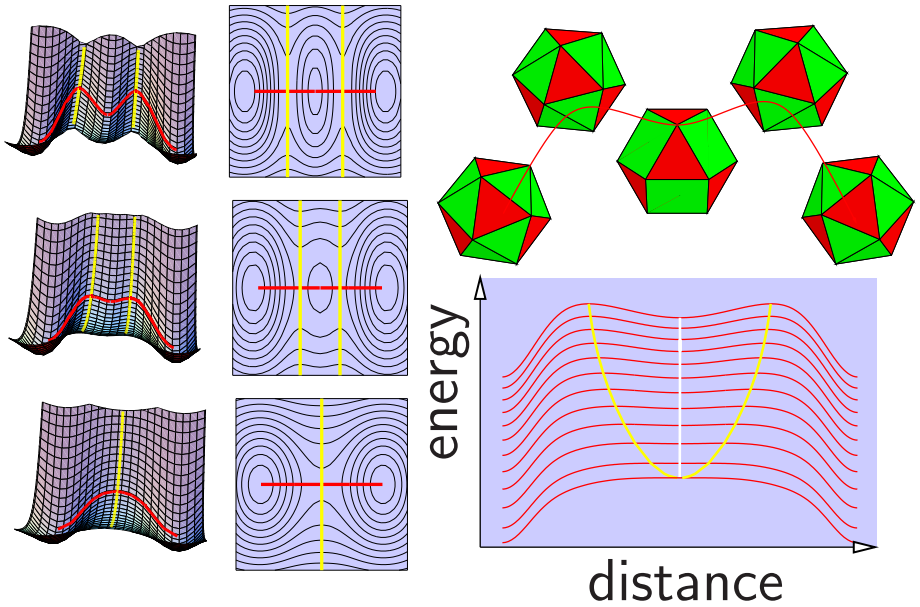

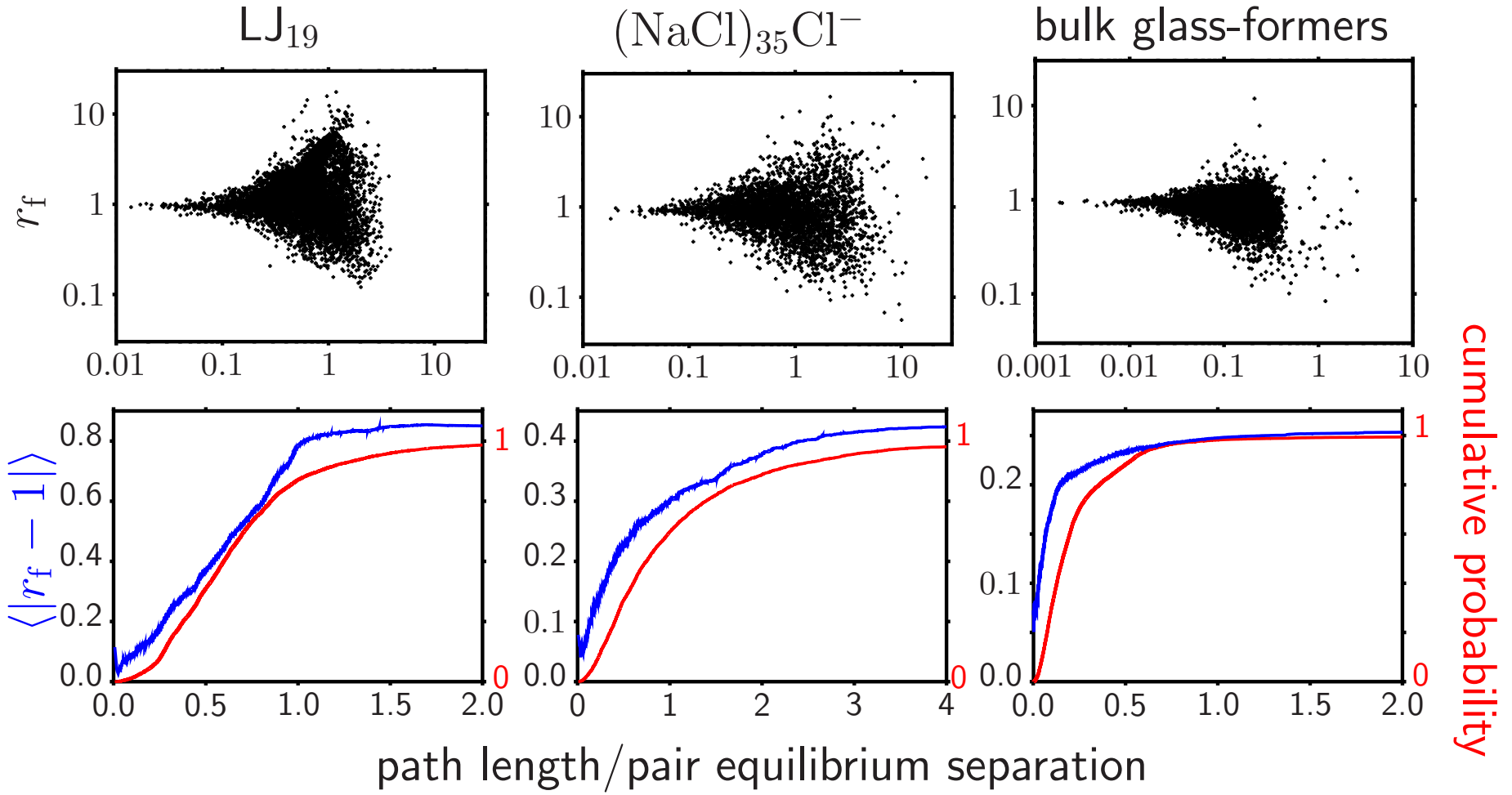

For a fixed potential we effectively have a snap-shot of parameter space. In bulk systems numerous minima separated by very small barriers have been characterised.[1,4] These two-level systems generally obey $r_f \approx 1$.

Software for Exploring and Visualising Landscapes

Non-commercial use is permitted under the Gnu General Public License.

- GMIN: basin-hopping global optimisation and global thermodynamics.
- OPTIM: geometry optimisation, including a wide variety of minimisation schemes and transition state algorithms. Multi-step pathways exploit the Dijkstra missing connection algorithm.[25]
- PATHSAMPLE: discrete path sampling refinement of kinetic transition networks. Recursive regrouping (lumping) based on free energy barriers. Extraction of committor probabilities and overall rate constants.
- disconnectionDPS and manipulate: creation and transformation of potential and free energy disconnectivity graphs from PATHSAMPLE output files.

Current svn tarball image: http://www-wales.ch.cam.ac.uk. Direct access to the svn source tree can be arranged for developers.

1. D. J. Wales, *Energy Landscapes*, Cambridge University Press, Cambridge (2003).
2. O. M. Becker and M. Karplus, J. Chem. Phys. **106**, 1495 (1997).
3. D. J. Wales, M. A. Miller and T. R. Walsh, Nature **394**, 758 (1998).
4. D. J. Wales, Science **293**, 2067 (2001).
5. D. J. Wales, Phil. Trans. Roy. Soc. A **363**, 357 (2005).
6. D. J. Wales and T. V. Bogdan, J. Phys. Chem. B **110**, 20765 (2006).
7. M. A. Miller and D. J. Wales, J. Chem. Phys. **111**, 6610 (1999).
8. D. J. Wales and P. E. J. Dewsbury, J. Chem. Phys. **121**, 10284 (2004).
9. D. J. Wales, J. Chem. Soc., Faraday Trans. **88**, 653 (1992).
10. D. J. Wales, J. Chem. Soc., Faraday Trans. **89**, 1305 (1993).
11. L. J. Munro and D. J. Wales, Phys. Rev. B **59**, 3969 (1999).
12. A. F. Voter, J. Chem. Phys. **106**, 4665 (1997).
13. G. Henkelman and H. Jónsson, J. Chem. Phys. **111**, 7010 (1999).
14. Y. Kumeda, L. J. Munro and D. J. Wales, Chem. Phys. Lett. **341**, 185 (2001).
15. J. P. K. Doye and D. J. Wales, J. Chem. Phys. **116**, 3777 (2002).
16. D. J. Wales and J. P. K. Doye, J. Chem. Phys. **119**, 12409 (2003).
17. J. P. K. Doye and D. J. Wales, J. Chem. Phys. **118**, 5263 (2003).
18. K. Müller and L. D. Brown, Theor. Chim. Acta **53**, 75 (1979).
19. L. R. Pratt, J. Chem. Phys. **85**, 5045 (1986).

20. R. Elber and M. Karplus, Chem. Phys. Lett. **139**, 375 (1987).
21. R. Czerminski and R. Elber, J. Chem. Phys. **92**, 5580 (1990).
22. G. Mills and H. Jónsson, Phys. Rev. Lett. **72**, 1124 (1994).
23. G. Henkelman and H. Jónsson, J. Chem. Phys. **113**, 9978 (2000).
24. S. A. Trygubenko and D. J. Wales, J. Chem. Phys. **120**, 2082 (2004).
25. J. M. Carr, S. A. Trygubenko and D. J. Wales, J. Chem. Phys. **122**, 234903 (2005).
26. D. J. Wales and J. P. K. Doye, J. Phys. Chem. A **101**, 5111 (1997).
27. J. P. K. Doye and D. J. Wales, Phys. Rev. Lett. **80**, 1357 (1998).
28. D. J. Wales and S. Ulker, Phys. Rev. B **74**, 212101 (2006).
29. D. J. Wales, H. McKay and E. L. Altschuler, Phys. Rev. B **79**, 224115 (2009).
30. T. V. Bogdan, D. J. Wales and F. Calvo, J. Chem. Phys. **124**, 044102 (2006).
31. B. Strodel and D. J. Wales, Chem. Phys. Lett. **466**, 105 (2008).
32. F. Noé and S. Fischer, Curr. Op. Struct. Biol. **18**, 154 (2008).
33. J. N. Murrell and K. J. Laidler, Trans. Faraday. Soc. **64**, 371 (1968).
34. H. Pelzer and E. Wigner, Z. Phys. Chem. **B15**, 445 (1932).
35. W. H. Miller, Acc. Chem. Res. **9**, 306 (1976).
36. D. J. Wales, Mol. Phys. **100**, 3285 (2002).
37. D. J. Wales, Mol. Phys. **102**, 891 (2004).
38. F. Calvo, T. V. Bogdan, V. K. de Souza and D. J. Wales, J. Chem. Phys. **127**, 044508 (2007).

39. D. J. Wales and J. P. K. Doye, Phys. Rev. B **63**, 214204 (2001).
40. R. G. Palmer, Adv. Phys. **31**, 669 (1982).
41. J. C. Mauro, P. K. Gupta and R. J. Loucks, J. Chem. Phys. **126**, 184511 (2007).
42. S. K. Ma, *Statistical mechanics*, World Scientific, Singapore (1985).
43. S. Sastry, P. G. Debenedetti and F. H. Stillinger, Nature **393**, 554 (1998).
44. C. A. Angell, Science **267**, 1924 (1995).
45. N. P. Kopsias and D. N. Theodorou, J. Chem. Phys. **109**, 8573 (1998).
46. T. F. Middleton and D. J. Wales, Phys. Rev. B **64**, 024205 (2001).
47. T. F. Middleton and D. J. Wales, J. Chem. Phys. **118**, 4583 (2003).
48. G. T. Barkema and N. Mousseau, Phys. Rev. Lett. **77**, 4358 (1996).
49. G. T. Barkema and N. Mousseau, Phys. Rev. Lett. **81**, 1865 (1998).
50. N. Mousseau and G. T. Barkema, Phys. Rev. E **57**, 2419 (1998).
51. G. T. Barkema and N. Mousseau, Computational Physics Communications **122**, 206 (1999).
52. J. C. Mauro, R. J. Loucks and J. Balakrishnan, J. Phys. Chem. B **110**, 5005 (2006).
53. B. Doliwa and A. Heuer, cond-mat/0209139 (2002).
54. B. Doliwa and A. Heuer, Phys. Rev. E **67**, 030501 (2003).
55. A. Saksaengwijit, B. Doliwa and A. Heuer, J. Phys. Cond. Matt. **15**, S1237 (2003).
56. V. K. de Souza and D. J. Wales, J. Chem. Phys. **129**, 164507 (2008).
57. D. Thirumalai and R. D. Mountain, Phys. Rev. E **47**, 479 (1993).

58. V. K. de Souza and D. J. Wales, J. Chem. Phys. **123**, 134504 (2005).
59. V. K. de Souza and D. J. Wales, Phys. Rev. B **74**, 134202 (2006).
60. V. K. de Souza and D. J. Wales, Phys. Rev. Lett. **96**, 057802 (2006).
61. V. K. de Souza and D. J. Wales, J. Chem. Phys. **130**, 194508 (2009).
62. G. S. Hammond, J. Am. Chem. Soc. **77**, 334 (1955).